

1 **Holocene climates of the Iberian Peninsula: pollen-based reconstructions of changes in**  
2 **the west-east gradient of temperature and moisture**

3 Mengmeng Liu<sup>1,\*</sup>, Yicheng Shen<sup>2</sup>, Penelope González-Sampéris<sup>3</sup>, Graciela Gil-Romera<sup>3</sup>,  
4 Cajo J. F. ter Braak<sup>4</sup>, Iain Colin Prentice<sup>1</sup>, Sandy P. Harrison<sup>2</sup>

5 1: Department of Life Sciences, Imperial College London, Silwood Park Campus, Buckhurst  
6 Road, Ascot SL5 7PY, UK

7 2: Geography & Environmental Science, Reading University, Whiteknights, Reading, RG6  
8 6AH, UK

9 3: Instituto Pirenaico de Ecología-CSIC, Avda. Montañana 1005, 50059, Zaragoza, Spain

10 4: Biometris (Applied Mathematics and Applied Statistics Centre), Wageningen University &  
11 Research, 6708 PB Wageningen, The Netherlands

12 \*: Corresponding author: Mengmeng Liu (m.liu18@imperial.ac.uk)

13 Ms for: *Climate of the Past*

14 **Abstract**

15 The Iberian Peninsula is characterised by a steep west-east moisture gradient today, reflecting  
16 the dominance of maritime influences along the Atlantic coast and more Mediterranean-type  
17 climate further east. Holocene pollen records from the Peninsula suggest that this gradient was  
18 less steep during the mid-Holocene, possibly reflecting the impact of orbital changes on  
19 circulation and thus regional patterns in climate. Here we use 7214 pollen samples from 117  
20 sites covering part or all of the last 12,000 years to reconstruct changes in seasonal temperature  
21 and in moisture across the Iberian Peninsula quantitatively. We show that there is an increasing  
22 trend in winter temperature at a regional scale, consistent with known changes in winter  
23 insolation. However, summer temperatures do not show the decreasing trend through the  
24 Holocene that would be expected if they were a direct response to insolation forcing. We show  
25 that summer temperature is strongly correlated with plant-available moisture ( $\alpha$ ), as measured  
26 by the ratio of actual evapotranspiration to equilibrium evapotranspiration, which declines  
27 through the Holocene. The reconstructions also confirm that the west-east gradient in moisture  
28 was considerably less steep than today during the mid-Holocene, indicating that atmospheric  
29 circulation changes (possibly driven by orbital changes) have been important determinants of  
30 the Holocene climate of the region.

## 31 **1. Introduction**

32 The Iberian Peninsula is characterised by a steep west-east gradient in temperature and  
33 moisture today, reflecting the dominance of maritime influences along the Atlantic coast and  
34 more Mediterranean-type climate further east. Projections of future climate change suggest that  
35 the region will become both warmer and drier, but nevertheless show that this west-east  
36 differentiation is maintained (Andrade et al., 2021a). The changes in temperature are projected  
37 to be larger and the occurrence of extreme temperature episodes more frequent in the south-  
38 central and eastern parts of Iberia than in Atlantic coastal areas (Carvalho et al., 2021). Similar  
39 gradients are seen in future projections of precipitation change, with largest reductions in  
40 precipitation in the south-central region (Andrade et al., 2021b). However, the stability of these  
41 west-east gradients during the Holocene has been questioned. In particular, the west-east  
42 gradient in moisture appears to have been less pronounced during the mid-Holocene (8~4 ka)  
43 when cooler summers and wetter conditions in the Atlantic zone (e.g. Martínez-Cortizas et al.,  
44 2009; Mauri et al., 2015) coincided with the maximum development of mesophytic vegetation  
45 further east and south (Aranbarri et al., 2014, 2015; Carrión et al., 2010, 2009; González-  
46 Sampériz et al., 2017).

47 However, much of the evidence for Holocene climates of the Iberian Peninsula is based on  
48 qualitative interpretations of vegetation changes, generally interpreted as reflecting changes in  
49 moisture availability (Morellón et al., 2018; Ramos-Román et al., 2018; Schröder et al., 2019).  
50 These records are extensive and they seem to indicate fairly complex spatial patterns of change.  
51 Kaufman et al. (2020) provides quantitative reconstructions of summer and winter temperature  
52 in their compilation of Holocene climate information, but there are only 5 terrestrial sites from  
53 the Iberian Peninsula. Iberia was also included in the quantitative pollen-based reconstructions  
54 of European climate through the Holocene in Mauri et al. (2015), which is an update of Davis  
55 et al. (2003). However, the geographical distribution of sites included is uneven and a large  
56 fraction of the records were from the Pyrenees and the Cantabrian mountains, with additional  
57 clustering of sites in coastal regions. Thus, the inferred patterns of climate over most of the  
58 central part of the Peninsula are therefore largely extrapolated. Tarroso et al. (2016) has  
59 provided reconstructions of summer and winter temperature and mean annual precipitation  
60 since the Last Glacial Maximum for the Iberian Peninsula, by using modern species distribution  
61 data to develop climate probability distribution functions (PDFs) and applying these to 31 fossil  
62 records. However, although they identified trends in precipitation during the Holocene, the

63 temperature reconstructions do not seem to be reliable since they show no changes through  
64 time (9~3 ka), either for the Iberian Peninsula as a whole or for individual sub-regions, in  
65 contradiction to the other reconstructions. The current state of uncertainty about Holocene  
66 climate changes in Iberia is further exacerbated because quantitative reconstructions of summer  
67 temperature made at individual sites using chironomid data (Muñoz Sobrino et al., 2013;  
68 Tarrats et al., 2018) are not consistent with reconstructed summer temperatures based on pollen  
69 for the same sites.

70 Here, using pollen-inferred transfer functions, we re-examine the trends in summer and winter  
71 temperature and plant-available moisture through the Holocene across Iberia, using a new and  
72 relatively comprehensive compilation of pollen data (Shen et al., 2022) with age models based  
73 on the latest radiocarbon calibration curve (IntCal20: Reimer et al., 2020). We explicitly test  
74 whether there are significant differences in the west-east gradient of moisture and temperature  
75 through time. We then analyse the relationships between the changes in the three climate  
76 variables and how trends in these variables are related to external climate forcing. These  
77 analyses allow us to investigate whether the west-east gradient in moisture was less steep  
78 during the mid-Holocene and explore what controls the patterns of climate change across the  
79 region.

## 80 **2. Methods**

81 Multiple techniques have been developed to make quantitative climate reconstructions from  
82 pollen (see reviews in Bartlein et al., 2011; Chevalier et al., 2020; Salonen et al., 2011). Modern  
83 analogue techniques (MAT: Overpeck et al., 1985) tend to produce rapid shifts in reconstructed  
84 values corresponding to changes in the selection of the specific analogue samples, although  
85 this tendency is less marked in the conceptually analogous response surface technique (Bartlein  
86 et al., 1986). Regression-based techniques, including weighted averaging methods such as  
87 Weighted Average Partial Least-Squares (WAPLS: ter Braak and Juggins, 1993), do not  
88 produce step-changes in the reconstructions but suffer from the tendency to compress the  
89 reconstructions towards the central part of the sampled climate range. However, this tendency  
90 can be substantially reduced by accounting for the sampling frequency ( $f_x$ ) and the climate  
91 tolerance of the pollen taxa present in the training data set ( $f_x$ TWA-PLS: Liu et al., 2020).  
92 Machine-learning and Bayesian approaches have also been applied to derive climate  
93 reconstructions from pollen assemblages (Peyron et al., 1998; Salonen et al., 2019). However,  
94 comparison of  $f_x$ TWA-PLS with the Bayesian model BUMPER (Holden et al., 2017), shows

95 that fxTWA-PLS performs better in capturing the climate of the modern training data set from  
96 Europe (Liu et al., 2020).

97 Although fxTWA-PLS has clear advantages over other quantitative reconstructions techniques,  
98 there is still a slight tendency towards compression. We have therefore made a further  
99 modification to the approach as described in Liu et al. (2020). In the original version of  
100 fxTWA-PLS, the fx correction is applied as a weight with the form of  $1/fx^2$  in the regression  
101 (step 7 in Table 1 in Liu et al., 2020). Here (see Appendix A) we make a further modification  
102 of fxTWA-PLS by (a) applying the fx correction separately in both the taxon calculation and  
103 the regression (step 2 and 7 in Table 1 in Liu et al., 2020) as a weight with the form of  $1/fx$  and  
104 (b) applying P-splines smoothing (Eilers and Marx, 2021) in order to reduce the dependence  
105 of the fx estimation on bin width. The modified version further reduces the biases at the  
106 extremes of the sampled climate range. We used this modified version of fxTWA-PLS to  
107 reconstruct three climate variables: mean temperature of the coldest month (MTCO), mean  
108 temperature of the warmest month (MTWA) and plant-available moisture represented by  $\alpha$ , an  
109 estimate of the ratio of actual evapotranspiration to equilibrium evapotranspiration. The  
110 individual and joint effects of MTCO, MTWA and  $\alpha$  were tested explicitly using canonical  
111 correspondence analysis (CCA). The modified version further reduces the biases at the  
112 extremes of the sampled climate range, while retaining the desirable properties of WA-PLS in  
113 terms of robustness to spatial autocorrelation (fxTWA-PLS: Liu et al., 2020).

114 The modern pollen training dataset was derived from the SPECIAL Modern Pollen Data Set  
115 (SMPDS: Harrison, 2019). The SMPDS consists of relative abundance records from 6458  
116 terrestrial sites from Europe, northern Africa, the Middle East and northern Eurasia (SI Fig.  
117 S1) assembled from multiple different published sources. The pollen records were  
118 taxonomically standardized, and filtered (as recommended by Chevalier et al., 2020) to remove  
119 obligate aquatics, insectivorous species, introduced species, and taxa that only occur in  
120 cultivation (see SI Table S1 for the list). Taxa (mainly herbaceous) with only sporadic  
121 occurrences were amalgamated to higher taxonomic levels (genus, sub-family or family) after  
122 ensuring consistency with their distribution in climate space. As a result of these  
123 amalgamations, the SMPDS contains data on 247 pollen taxa. For our analysis, we use the 195  
124 taxa that occur at more than 10 sites.

125 Modern climate data at each of the sites in the training data set were obtained from Harrison  
126 (2019). This data set contains climate reconstructions of MTCO, growing degree days above a

127 baseline of  $0^{\circ}\text{C}$  ( $\text{GDD}_0$ ) and a moisture index (MI), defined as the ratio of annual precipitation  
128 to annual potential evapotranspiration. The climate at each site was obtained using  
129 geographically-weighted regression of the CRU CL v2.0 gridded dataset of modern (1961-  
130 1990) surface climate at 10 arc minute resolution (New et al., 2002) in order to correct for  
131 elevation differences between each pollen site and the corresponding grid cell. The  
132 geographically-weighted regression used a fixed bandwidth kernel of  $1.06^{\circ}$  ( $\sim 140\text{km}$ ) to  
133 optimize model diagnostics and reduce spatial clustering of residuals relative to other  
134 bandwidths. The climate of each pollen site was then estimated based on its longitude, latitude,  
135 and elevation. MTCO and  $\text{GDD}_0$  was taken directly from the GWR regression and MI was  
136 calculated for each pollen site using a modified code from SPLASH v1.0 (Davis et al., 2017)  
137 based on daily values of precipitation, temperature and sunshine hours again obtained using a  
138 mean-conserving interpolation of the monthly values of each. For this application, we used  
139 MTCO directly from the data set but calculated MTWA from MTCO and  $\text{GDD}_0$ , based on the  
140 relationship between MTCO, MTWA and  $\text{GDD}_0$  given by Appendix 2 of Wei et al. (2021).  
141 We derived  $\alpha$  from MI following Liu et al. (2020). The modern training data set provides  
142 records spanning a range of MTCO from  $-42.4^{\circ}\text{C}$  to  $14.8^{\circ}\text{C}$ , of MTWA from  $4.2^{\circ}\text{C}$  to  $33.5$   
143  $^{\circ}\text{C}$ , and of  $\alpha$  from 0.04 to 1.25 (Fig. 1, SI Fig. S1).

144 The fossil pollen data from the Iberian Peninsula were compiled by Shen et al. (2021) and the  
145 data set was obtained from Harrison et al. (2022). The taxonomy used by Shen et al. (2021) is  
146 consistent with that employed in the SMPDS. Shen et al. (2021) provides consistent age models  
147 for all the records based on the IntCal20 calibration curve (Reimer et al., 2020) and the BACON  
148 Bayesian age-modelling tool (Blaauw et al., 2021; Blaauw and Christeny, 2011) using the  
149 supervised modelling approach implemented in the `ageR` package (Villegas-Diaz et al, 2021).  
150 We excluded individual pollen samples with large uncertainties (standard error larger than 100  
151 years) on the attributed in the new age model. As a result, the climate reconstructions are based  
152 on a fossil data set of 7384 pollen samples from 117 records covering part or all of the last  
153 12,000 years (Fig. 2), with 42 individual records provided by the original authors, 73 records  
154 obtained from the European Pollen Database (EPD, [www.europeanpollendatabase.net](http://www.europeanpollendatabase.net)) and 2  
155 records from PANGAEA ([www.pangaea.de/](http://www.pangaea.de/)). Details of the records are given in Table 1. The  
156 average temporal resolution of these records is 101 years. We then excluded a few samples  
157 where the reconstructed values of  $\alpha$  exceed the natural limit of 0 and 1.26. Finally, 7214  
158 samples from 117 records are used for the analyses of the climate reconstructions. Summer  
159 insolation and winter insolation are also calculated using the PAST software based on the age

160 and latitude of each sample (Hammer et al., 2001).

161 Variance inflation factor (VIF) scores are calculated for both the modern climates and the  
162 climates reconstructed from fossil pollen records, in order to avoid multicollinearity problems  
163 and thus guarantee the climate variables (MTCO, MTWA,  $\alpha$ ) used here represent independent  
164 features of the pollen records.

165 In addition to examining the reconstructions for individual sites, we constructed composite  
166 curves for the Iberian Peninsula as a whole. The composite curves provide a way of comparing  
167 the relationship between trends in the reconstructed climate changes and insolation changes.  
168 The curves were constructed after binning the site-based reconstructions using  $\pm 500$ -year bins.  
169 We did 1000 bootstrap resampling of the reconstructed climate values in each  $\pm 500$ -year bin  
170 to avoid the influence of a single value or a single site on the mean climate value in this bin,  
171 and use the standard deviation of the 1000 values to represent the uncertainty of the mean  
172 climate value. We constructed linear regression plots to examine the longitudinal and  
173 elevational patterns in the reconstructed climate variables, and assessed the significance of  
174 differences in these trends through time compared to the most recent bin ( $0.5 \text{ ka} \pm 500 \text{ years}$ )  
175 based on  $p$  values, with the customary threshold of 0.05. We then compared the climate trends  
176 with changes in summer and winter insolation.

### 177 **3. Results**

178 The modified version of fxTWA-PLS reproduces the modern climate reasonably well (Table  
179 2). The performance is best for MTCO ( $R^2$  0.75, RMSEP 4.70, slope 0.91) but is also good for  
180  $\alpha$  ( $R^2$  0.68, RMSEP 0.16, slope 0.78) and MTWA ( $R^2$  0.57, RMSEP 3.47, slope 0.71). The  
181 correlations between pollen records and each of the three bioclimate variables, as assessed by  
182 CCA, were strong for both modern climate data and fossil reconstructions (Table 3). The  
183 variance inflation factor (VIF) scores are all less than 6, so there are no multicollinearity  
184 problems (Table 3) (Allison, 1994). Furthermore, the taxa that contribute most strongly to  
185 reconstructing colder/warmer or wetter/drier climates show predictable patterns consistent with  
186 their known ecological preferences (SI Table S2).

187 Winters were generally colder than present during the early to mid-Holocene, as shown by the  
188 coherent patterns of reconstructed anomalies at individual sites (Fig. 3a, 3d). Here “present”  
189 means the most recent pollen bin ( $0.5 \text{ ka} \pm 500 \text{ years}$ ). The composite curve also shows a  
190 general increase in winter temperatures through time (Fig. 4a), consistent with the trend in

191 winter insolation (Fig. 4d). The composite curve shows that it was ca 4°C cooler than today at  
192 11.5 ka and conditions remained cooler than present until ca 2.5 ka. Winter temperatures today  
193 increase from north to south and are also affected by elevation; these patterns are still present  
194 in the Holocene reconstructions, but there is no spatial differentiation between western and  
195 eastern Iberia in the anomalies (Table 4, SI Fig. S2). The similarity of the changes compared  
196 to present geographically is consistent with the idea that the changes in winter temperature are  
197 driven by changes in winter insolation.

198 Summers were somewhat hotter than present in the west and cooler than present in the east  
199 during the early and mid-Holocene, as shown by the reconstructed anomalies at individual sites  
200 (Fig. 3b, 3e). This west-east difference could not arise if the changes in summer temperatures  
201 were a direct reflection of the insolation forcing (Fig. 4e). Indeed, the composite curve shows  
202 relatively little change in MTWA (Fig. 4b), confirming that there is no direct relationship to  
203 insolation forcing (Fig. 4e).

204 There is a strong west-east gradient in  $\alpha$  at the present day (Fig. 2), with wetter conditions in  
205 the west and drier conditions in the east. However, the reconstructed anomalies at individual  
206 sites (Fig. 3c, 3f) suggest that west was drier and the east was wetter than present in the mid-  
207 Holocene, resulting in a flatter west-east gradient. The west-east gradient is significantly  
208 different from present between 9.5 ~ 3.5 ka (Fig. 5, Table 4), implying stronger moisture  
209 advection into the continental interior during the mid-Holocene. The change in gradient is seen  
210 in both high and low elevation sites (SI Fig. S3). There is also significant change in  $\alpha$  with  
211 elevation between 9.5 ~ 4.5 ka (Table 4, SI Fig. S4).

212 Summer temperatures are strongly correlated with changes in  $\alpha$ , both in terms of spatial  
213 correlations in the modern data set at a European scale and in terms of spatial and temporal  
214 correlations the fossil data set from Iberian Peninsula (Fig. 6). The patterns of reconstructed  
215 anomalies in MTWA and  $\alpha$  at individual sites are also coherent (Fig. 3b, 3c, 3e, 3f), showing  
216 drier conditions and hotter summers than present in the west and wetter conditions with cooler  
217 summers in the east during the early to mid-Holocene. The west-east gradient in MTWA was  
218 significantly different from present between 9.5 and 3.5 ka except 8.5 ka (Table 4, SI Fig. S5),  
219 roughly the interval when the gradient in  $\alpha$  was also significantly different from present. Again,  
220 the change in the east-west gradient is registered at both high and low elevation sites (SI Fig.  
221 S6). However, there is no significant change in MTWA with elevation except 8.5 and 7.5 ka  
222 (Table 4, SI Fig. S7).

#### 223 4. Discussion

224 We have shown that there was a gradual increase in MTCO over the Holocene, both for most  
225 of the individual sites represented in the data set and for Iberia as a whole. Colder winters in  
226 southern Europe during the mid-Holocene (6 ka) are a feature of many earlier reconstructions  
227 (e.g. Cheddadi et al., 1997; Wu et al., 2007). A general warming trend over the Holocene is  
228 seen in gridded reconstructions of winter season (December, January, February) temperatures  
229 as reconstructed using the modern analogue approach by Mauri et al. (2015), although there is  
230 somewhat less millennial-scale variability in these reconstructions (Fig. 7). Nevertheless, their  
231 reconstructions show a cooling of 3°C in the early Holocene, comparable in magnitude to the  
232 ca 4°C cooling at 11.5 ka reconstructed here. Although they show conditions slightly cooler  
233 than present persisting up to 1 ka, the differences are very small (ca 0.5°C) after 2 ka, again  
234 consistent with our reconstructions of MTCO similar to present by 2.5 ka. Quantitative  
235 reconstructions of winter temperature for the 5 terrestrial sites from the Iberian Peninsula in  
236 the Kaufman et al. (2020) compilation all show a general trend of winter warming over the  
237 Holocene, but the magnitude of the change at some of the individual sites is much larger (ca  
238 10°C) and there is no assessment of the uncertainty on these reconstructions. The composite  
239 curve of Kaufman et al. (2020) shows an increasing trend in MTCO through the Holocene  
240 although with large uncertainties (Fig. 7). In contrast to the consistency of the increasing trend  
241 in MTCO during the Holocene between our reconstructions and those of Mauri et al. (2015)  
242 and Kaufman et al. (2020), there is no discernible trend in MTCO during the Holocene  
243 reconstruction of Tarroso et al. (2016). Indeed, there is no significant change in their MTCO  
244 values after ca 9 ka, either for the Peninsula as a whole (Fig. 7) or for any of the four sub-  
245 regions they considered. Our reconstructed trend in winter temperature is consistent with the  
246 changes in insolation forcing at this latitude during the Holocene, and is also consistent with  
247 transient climate model simulations (Braconnot et al., 2019; Carré et al., 2021; Dallmeyer et  
248 al., 2020; Parker et al., 2021) of the winter temperature response to changing insolation forcing  
249 over the late Holocene in this region (Fig. 8, SI Fig. S8). Thus, we suggest that changes in  
250 winter temperatures are a direct consequence of insolation forcing.

251 We have shown that there is no overall trend in MTWA during the Holocene. According to our  
252 reconstructions, summer temperatures fluctuated between ca 0.5°C above or below modern  
253 temperature. The lack of coherent trend in MTWA is consistent with the gridded  
254 reconstructions of summer (June, July, August) temperature in the Mauri et al. (2015) data set  
255 and also with the 5 terrestrial sites from Iberia included in the Kaufman et al. (2020) data set.



256 However, the patterns shown in the three data sets are very different from one another. Mauri  
257 et al. (2015) suggest the early Holocene was colder than today, and although temperatures  
258 similar to today were reached at 9 ka, most of the Holocene was characterised by cooler  
259 summers. Kaufman et al. (2020), however, showed warmer than present conditions during the  
260 early Holocene although they also show cooler conditions during the later Holocene. The  
261 differences between the three data sets could reflect differences in the reconstruction methods,  
262 or differences in the number of records used and in the geographic sampling. However, given  
263 the fact that all three data sets show similar trends in winter temperature, the lack of coherency  
264 between the data sets for MTWA points to there not being a strong, regionally coherent signal  
265 of summer temperature changes during the Holocene. Tarroso et al. (2016) also showed no  
266 significant changes in MTWA after ca 9 ka (Fig. 7).

267 The chironomid record from Laguna de la Roya covers the late glacial and terminates at 10.5  
268 ka (Muñoz Sobrino et al., 2013). The reconstructed July temperature during the early Holocene  
269 is ca 12~13 °C, which is considerably cooler than today at this site. However, the authors  
270 caution that these samples have poor analogues and the record should be interpreted with  
271 caution. Chironomid-based reconstructions of July temperature at Basa de la Mora (Tarrats et  
272 al., 2018), a high elevation site in the Pyrenees, indicate temperatures within  $\pm 0.5^\circ \text{C}$  of the  
273 modern during the early to mid-Holocene (10~6 ka), similar to our regional composite  
274 reconstructions. However, they show persistently conditions cooler than present by ca 1.5 °C  
275 between 4.5 and 2 ka, not seen in our reconstructions. Furthermore, direct comparison of our  
276 reconstructions of MTWA at Basa de la Mora (SI Fig. S9) to the chironomid-based  
277 reconstructions highlights that the two records show very different trajectories, since the  
278 pollen-based reconstruction of this site shows a consistent warming trend throughout the  
279 Holocene. Although Tarrats et al. (2018) argue that discrepancies between their temperature  
280 reconstructions and pollen-based reconstructions reflects the fact that the vegetation of Iberia,  
281 including the mountain areas, is largely driven by moisture changes and perhaps is not a good  
282 indicator of temperature, we have shown that there is sufficient information in the pollen  
283 records to reconstruct temperature and moisture independently (Table 3, Table S2). Thus, the  
284 cause of the differences between the pollen-based and chironomid-based reconstructions at  
285 Basa de la Mora is presumably related to methodology. In particular, the chironomid  
286 reconstructions use a training data set that does not include samples from the Pyrenees, or  
287 indeed the Mediterranean more generally, and may therefore not provide good analogues for  
288 Holocene changes at this site.

289 The lack of a clear trend in MTWA in our reconstructions is not consistent with insolation  
290 forcing, which shows a declining trend during the Holocene nor is it consistent with simulated  
291 changes in MTWA in transient climate model simulations of the summer temperature response  
292 to changing insolation forcing over the Holocene in this region (Fig. 8). The change in moisture  
293 gradient during the mid-Holocene, however, suggests an alternative explanation whereby  
294 changes in summer temperature are a response to land-surface feedbacks associated with  
295 changes in moisture. Specifically, the observed increased advection of moisture into eastern  
296 Iberia would have created wetter conditions there, which in turn would permit increased  
297 evapotranspiration, implying less allocation of available net radiation to sensible heating, and  
298 resulting in cooler air temperatures. Our reconstructions show that the west-east moisture  
299 gradient in mid-Holocene was significantly flatter than the steep moisture gradient today,  
300 implying a significant increase in moisture advection into the continental interior during this  
301 period. Mauri et al. (2015) also showed that summers were generally wetter than present in the  
302 east but drier than present in the west at early to mid-Holocene, supporting the idea of a flatter  
303 west-east gradient.

304 We have shown that stronger moisture advection is not a feature of transient climate model  
305 simulations of the Holocene, which may explain why these simulations do not show a strong  
306 modification of the insolation-driven changes in summer temperature (Fig. 8). Although the  
307 amplitude differs, all of the models show a general decline in summer temperature. The failure  
308 of the current generation of climate models to simulate the observed strengthening of moisture  
309 transport into Europe and Eurasia during the mid-Holocene has been noted for previous  
310 versions of these models (e.g. Bartlein et al., 2017; Mauri et al., 2014) and also shown in Fig.  
311 S8. Mauri et al. (2014), for example, showed that climate models participating in the last phase  
312 of the Coupled Model Intercomparison Project (CMIP5/PMIP3) were unable to reproduce  
313 reconstructed climate patterns over Europe at 6000 yr B.P. and indicated that this resulted from  
314 over-sensitivity to changes in insolation forcing and the failure to simulate increased moisture  
315 transport into the continent. Bartlein et al. (2017) showed that the CMIP5/PMIP3 models  
316 simulated warmer and drier conditions in mid-continental Eurasia at 6000 yr B.P., inconsistent  
317 with palaeo-environmental reconstructions from the region, as a result of the simulated  
318 reduction in the zonal temperature gradient which resulted in weaker westerly flow and reduced  
319 moisture fluxes into the mid-continent. They also pointed out the strong feedback between drier  
320 conditions and summer temperatures. The drying of the mid-continent is also a strong feature  
321 of the mid-Holocene simulations made with the current generation of CMIP6/PMIP4 models

322 (Brierley et al., 2020). The persistence of these data-model mismatches highlights the need for  
323 better modelling of land-surface feedbacks on atmospheric circulation and moisture.

324 There are comparatively few pollen-based reconstructions of moisture changes during the  
325 Holocene from Iberia. Records from Padul show increased mean annual and winter  
326 precipitation during the early and mid-Holocene (Camuera et al., 2022; García-Alix et al.,  
327 2021). Reconstructions of mean annual and winter precipitation (Camuera et al., 2022) and the  
328 ratio of annual precipitation to annual potential evapotranspiration (Wei et al., 2021) also show  
329 wetter conditions at this time at El Cañizar de Villarquemado. Both of these sites lie in the  
330 eastern part of the Iberian Peninsula, so these reconstructions are consistent with our  
331 interpretation of wetter conditions in this region during the interval between 9.5 and 3.5 ka.  
332 Ilvonen et al. (2022) provide pollen-based reconstructions of mean annual, summer and winter  
333 precipitation from 8 sites in Iberia, using WAPLS and a Bayesian modelling approach.  
334 Although they focus on the contrasting pattern of hydroclimate evolution between northern and  
335 southern Iberia, the three easternmost sites (San Rafael, Navarres, and Quintanar de la Sierra)  
336 show much wetter conditions during the early to mid-Holocene. With the exception of the  
337 record from Monte Areo, the records from further west are relatively complacent and indeed  
338 two sites (Zalamar, El Maillo) show decreased precipitation between 8 and 4 ka. Thus, these  
339 records are consistent with our interpretation that the west-east gradient of moisture was  
340 reduced between 9.5 and 4.5 ka.

341 Speleothem oxygen-isotope data from the Iberian Peninsula provide support for our pollen-  
342 based reconstructions of changes in the west-east gradient of moisture through the Holocene.  
343 The speleothem records show a progressive increase in temperature from the Younger Dryas  
344 onwards, although the trend is less marked in the west than the east (Baldini et al., 2019). This  
345 warming trend is consistent with our reconstructions of changes in MTCO through the  
346 Holocene. Speleothem records also show distinctly different patterns in moisture availability,  
347 with sites in western Iberia indicating wetter environments during early Holocene and a  
348 transition to drier conditions from ca 7.5 cal ka BP to the present (Stoll et al., 2013; Thatcher  
349 et al., 2020) while eastern sites record wetter conditions persisting from 9 to 4 cal ka (Walczak  
350 et al., 2015). This finding would support the weaker west to east moisture gradient shown by  
351 our results.

352 Pollen data are widely used for the quantitative reconstruction of past climates (see discussion  
353 in Bartlein et al., 2011), but reconstructions of moisture indices are also affected by changes in

354 water-use efficiency caused by the impact of changing atmospheric CO<sub>2</sub> levels on plant  
355 physiology (Farquhar, 1997; Gerhart and Ward, 2010; Prentice et al., 2017; Prentice and  
356 Harrison, 2009). This has been shown to be important on glacial-interglacial timescales, when  
357 intervals of lower-than-present CO<sub>2</sub> result in vegetation appearing to reflect drier conditions  
358 than were experienced in reality (Prentice et al., 2011, 2017; Wei et al., 2021). We do not  
359 account for this CO<sub>2</sub> effect in our reconstructions of  $\alpha$  because the change in CO<sub>2</sub> over the  
360 Holocene was only 40 ppm. This change relative to modern levels has only a small impact on  
361 the reconstructions (Prentice et al., 2022) and is sufficiently small to be within the  
362 reconstruction uncertainties. Furthermore, accounting for changes in CO<sub>2</sub> would not affect the  
363 reconstructed west-east gradient through time.

364 A more serious issue for our reconstructions may be the extent to which the vegetation cover  
365 of Iberia was substantially modified by human activities during the Holocene. Archaeological  
366 evidence shows that the introduction of agriculture during the Neolithic transition occurred ca  
367 7.6 ka in some southern and eastern areas of the Iberian Peninsula but spread slowly and  
368 farming first occurred only around 6 ka in the northwest (Drake et al., 2017; Fyfe et al., 2019;  
369 Zapata et al., 2004). Anthropogenic changes in land use have been detected at a number of  
370 sites, based on pollen evidence of increases in weeds or the presence of cereals (e.g. Abel-  
371 Schaad and López-Sáez, 2013; Cortés Sánchez et al., 2012; López-Merino et al., 2010; Mighall  
372 et al., 2006; Peña-Chocarro et al., 2005) or the presence of fungal spores associated with animal  
373 faeces which has been used to identify the presence of domesticated animals (e.g. López-Sáez  
374 and López-Merino, 2007; Revelles et al., 2018). The presence of cereals is the most reliable  
375 source of data on human activities, but most cereals only release pollen during threshing and  
376 thus are not found in abundance in pollen diagrams from natural (as opposed to archaeological)  
377 sites (Trondman et al., 2015). Indeed, it is only after ca 1 ka that the number of sites which  
378 record cereal pollen exceeds the number of sites at which cereals are not represented (Githumbi  
379 et al., 2022). Thus, while anthropogenic activities may have been important at the local scale  
380 and particularly in the later Holocene (e.g. Connor et al., 2019; Fyfe et al., 2019; Githumbi et  
381 al., 2022), most of the sites used for our reconstructions are not associated with archaeological  
382 evidence of agriculture or substantial landscape modification. Furthermore, the consistency of  
383 the reconstructed changes in climate across sites provides support for these being largely a  
384 reflection of regional climate changes rather than human activities.

385

386 We have used a modified version of fxTWA-PLS to reconstruct Holocene climates of the  
387 Iberian Peninsula because this modification reduced the compression bias in MTCO and  
388 MTWA, and specifically reduces the maximum bias in MTCO, MTWA and  $\alpha$ . Although this  
389 modified approach produces better overall reconstructions (Appendix A), its use does not  
390 change the reconstructed trends in these variables through time (SI Fig. S10). Thus, the finding  
391 that winter temperatures are a direct reflection of insolation forcing whereas summer  
392 temperatures are influenced by land-surface feedbacks and changes in atmospheric circulation  
393 is robust to the version of fxTWA-PLS used. However, while we use a much larger data set  
394 than previous reconstructions, the distribution of pollen sites is uneven and the northern part  
395 of the Peninsula is better sampled than the southwest, which could lead to some uncertainties  
396 in the interpretation of changes in the west-east gradient of moisture. It would, therefore, be  
397 useful to specifically target the southwestern part of the Iberian Peninsula for new data  
398 collection. Alternatively, it would be useful to apply the approach used here to the whole of  
399 Eurasia, given that the failure of state-of-the-art climate models to advect moisture into the  
400 continental interior appears to be a feature of the whole region (Bartlein et al., 2017) and not  
401 the Peninsula alone.

## 402 **5. Conclusion**

403 We have developed an improved version of fxWA-PLS which further reduces compression  
404 bias and provides robust climate reconstructions. We have used this technique with a large  
405 pollen data set representing 117 sites across the Iberian Peninsula to make quantitative  
406 reconstructions of summer and winter temperature and an index of plant-available moisture  
407 through the Holocene. We show that there was a gradual increase in winter temperature through  
408 the Holocene and that this trend broadly follows the changes in orbital forcing. Summer  
409 temperatures, however, do not follow the changes in orbital forcing but appear to be influenced  
410 by land-surface feedbacks associated with changes in moisture. We show that the west-east  
411 gradient in moisture was considerably less pronounced during the mid-Holocene (8~4 ka),  
412 implying a significant increase in moisture advection into the continental interior resulting from  
413 changes in circulation. Our reconstructions of temperature changes are broadly consistent with  
414 previous reconstructions, but are more solidly based because of the increased site coverage.  
415 Our reconstructions of changes in the west-east gradient of moisture during the early part of  
416 the Holocene are also consistent with previous reconstructions, although this change is not  
417 simulated by state-of-the-art climate models, implying that there are still issues to resolve the

418 associated land-surface feedbacks in these models. Our work provides an improved foundation  
419 for documenting and understanding the Holocene palaeoclimates of Iberia.

420

421 **Data and Code Availability**

422 All the data used are public access and cited here. The code used to generate the climate  
423 reconstructions is available at <https://github.com/ml4418/Iberia-paper.git>.

424 **Supplement.** The supplement related to this article is available online.

425 **Competing interests.** We declare that we have no conflict of interest.

426 **Author Contributions.** ML, ICP and SPH designed the study. ML, ICP and CJFtB designed  
427 the modifications to fxTWA-PLS. PG-S and GG-R provided pollen data and insights into the  
428 regional palaeoclimate histories. ML carried out the analyses. ML and SPH wrote the first  
429 draft of the paper and all authors contributed to the final draft.

430 **Acknowledgements.** ML acknowledges support from Imperial College through the Lee  
431 Family Scholarship. YS and SPH acknowledge support from the ERC-funded project GC 2.0  
432 (Global Change 2.0: Unlocking the past for a clearer future; grant number 694481). ICP  
433 acknowledges support from the ERC under the European Union Horizon 2020 research and  
434 innovation programme (grant agreement no: 787203 REALM). This work is a contribution to  
435 the project "Origen y Cuantificación de los Cambios Paleoambientales en el Pirineo:  
436 Variabilidad climatic e impacto humano" (PYCACHU: PID2019-106050RB-I00)" funded by  
437 the Ministerio de Ciencia e Innovación.

438 **Financial support.** This research has been supported by Lee Family Scholarship fund, and  
439 the European Research Council (grant no. GC2.0, 694481, and grant no. REALM, 787203).

440 **References**

- 441 Abel-Schaad, D. and López-Sáez, J. A.: Vegetation changes in relation to fire history and  
 442 human activities at the Peña Negra mire (Bejar Range, Iberian Central Mountain System,  
 443 Spain) during the past 4,000 years, *Veg. Hist. Archaeobot.*, 22, 199–214,  
 444 doi:10.1007/s00334-012-0368-9, 2013.
- 445 Allison, P. D.: *Multiple Regression: A Primer*, Pine Forge Press., 1994.
- 446 Andrade, C., Contente, J. and Santos, J. A.: Climate change projections of aridity conditions  
 447 in the Iberian Peninsula, *Water*, 13(15), doi:10.3390/w13152035, 2021a.
- 448 Andrade, C., Contente, J. and Santos, J. A.: Climate change projections of dry and wet events  
 449 in Iberia based on the WASP-Index, *Climate*, 9(6), doi:10.3390/cli9060094, 2021b.
- 450 Aranbarri, J., Gonzalez Samperiz, P., Valero-Garcés, B., Moreno, A., Gil-Romera, G.,  
 451 Sevilla-Callejo, M., Garcia-Prieto, E., Di Rita, F., Mata, M. del Pi., Morellón, M., Magri, D.,  
 452 Rodriguez-Lazaro, J. and Carrión, J.: Rapid climatic changes and resilient vegetation during  
 453 the Lateglacial and Holocene in a continental region of south-western Europe, *Glob. Planet.*  
 454 *Change*, 114, 50–65, doi:10.1016/j.gloplacha.2014.01.003, 2014.
- 455 Aranbarri, J., González-Sampériz, P., Iriarte, E., Moreno, A., Rojo-Guerra, M., Peña-  
 456 Chocarro, L., Valero-Garcés, B., Leunda, M., García-Prieto, E., Sevilla-Callejo, M., Gil-  
 457 Romera, G., Magri, D. and Rodríguez-Lázaro, J.: Human–landscape interactions in the  
 458 Conquezueta–Ambrona Valley (Soria, continental Iberia): From the early Neolithic land use  
 459 to the origin of the current oak woodland, *Palaeogeogr. Palaeoclimatol. Palaeoecol.*, 436, 41–  
 460 57, doi:https://doi.org/10.1016/j.palaeo.2015.06.030, 2015.
- 461 Baldini, L. M., Baldini, J. U. L., McDermott, F., Arias, P., Cueto, M., Fairchild, I. J.,  
 462 Hoffmann, D. L., Matthey, D. P., Müller, W., Nita, D. C., Ontañón, R., García-Moncó, C. and  
 463 Richards, D. A.: North Iberian temperature and rainfall seasonality over the Younger Dryas  
 464 and Holocene, *Quat. Sci. Rev.*, 226, 105998,  
 465 doi:https://doi.org/10.1016/j.quascirev.2019.105998, 2019.
- 466 Bartlein, P. J., Prentice, I. C. and Webb, T.: Climatic response surfaces from pollen data for  
 467 some Eastern North American taxa, *J. Biogeogr.*, 13(1), 35, doi:10.2307/2844848, 1986.
- 468 Bartlein, P. J., Harrison, S. P., Brewer, S., Connor, S., Davis, B. A. S., Gajewski, K., Guiot,  
 469 J., Harrison-Prentice, T. I., Henderson, A., Peyron, O., Prentice, I. C., Scholze, M., Seppä, H.,  
 470 Shuman, B., Sugita, S., Thompson, R. S., Viau, A. E., Williams, J. and Wu, H.: Pollen-based  
 471 continental climate reconstructions at 6 and 21 ka: A global synthesis, *Clim. Dyn.*, 37(3),  
 472 775–802, doi:10.1007/s00382-010-0904-1, 2011.
- 473 Bartlein, P. J., Harrison, S. P. and Izumi, K.: Underlying causes of Eurasian midcontinental  
 474 aridity in simulations of mid-Holocene climate, *Geophys. Res. Lett.*, 44(17), 9020–9028,  
 475 doi:10.1002/2017GL074476, 2017.

- 476 Blaauw, M. and Christeny, J. A.: Flexible paleoclimate age-depth models using an  
477 autoregressive gamma process, *Bayesian Anal.*, 6(3), 457–474, doi:10.1214/11-BA618, 2011.
- 478 Blaauw, M., Christen, J. A., Lopez, M. A. A. V., V., J. E. O. M. G., Belding, T., Theiler, J.,  
479 Gough, B. and Karney, C.: rbacon: Age-depth modelling using Bayesian statistics, [online]  
480 Available from: <https://cran.r-project.org/package=rbacon>, 2021.
- 481 ter Braak, C. J. F. and Juggins, S.: Weighted averaging partial least squares regression (WA-  
482 PLS): An improved method for reconstructing environmental variables from species  
483 assemblages, *Hydrobiologia*, 269(1), 485–502, doi:10.1007/BF00028046, 1993.
- 484 Braconnot, P., Crétat, J., Marti, O., Balkanski, Y., Caubel, A., Cozic, A., Foujols, M.-A. and  
485 Sanogo, S.: Impact of multiscale variability on last 6,000 years Indian and West African  
486 monsoon rain, *Geophys. Res. Lett.*, 46(23), 14021–14029,  
487 doi:<https://doi.org/10.1029/2019GL084797>, 2019.
- 488 Brierley, C. M., Zhao, A., Harrison, S. P., Braconnot, P., Williams, C. J. R., Thornalley, D. J.  
489 R., Shi, X., Peterschmitt, J.-Y., Ohgaito, R., Kaufman, D. S., Kageyama, M., Hargreaves, J.  
490 C., Erb, M. P., Emile-Geay, J., D’Agostino, R., Chandan, D., Carré, M., Bartlein, P., Zheng,  
491 W., Zhang, Z., Zhang, Q., Yang, H., Volodin, E. M., Tomas, R. A., Routson, C., Peltier, W.  
492 R., Otto-Bliesner, B., Morozova, P. A., McKay, N. P., Lohmann, G., Legrande, A. N., Guo,  
493 C., Cao, J., Brady, E., Annan, J. D. and Abe-Ouchi, A.: Large-scale features and evaluation  
494 of the PMIP4-CMIP6 midHolocene simulations, *Clim. Past Discuss.*, 2020, 1–35,  
495 doi:10.5194/cp-2019-168, 2020.
- 496 Camuera, J., Ramos-Román, M. J., Jiménez-Moreno, G., García-Alix, A., Ilvonen, L., Ruha,  
497 L., Gil-Romera, G., González-Sampériz, P. and Seppä, H.: Past 200 kyr hydroclimate  
498 variability in the western Mediterranean and its connection to the African Humid Periods,  
499 *Sci. Rep.*, 12(1), 9050, doi:10.1038/s41598-022-12047-1, 2022.
- 500 Carré, M., Braconnot, P., Elliot, M., d’Agostino, R., Schurer, A., Shi, X., Marti, O.,  
501 Lohmann, G., Jungclaus, J., Cheddadi, R., Abdelkader di Carlo, I., Cardich, J., Ochoa, D.,  
502 Salas Gismondi, R., Pérez, A., Romero, P. E., Turcq, B., Corrège, T. and Harrison, S. P.:  
503 High-resolution marine data and transient simulations support orbital forcing of ENSO  
504 amplitude since the mid-Holocene, *Quat. Sci. Rev.*, 268, 107125,  
505 doi:<https://doi.org/10.1016/j.quascirev.2021.107125>, 2021.
- 506 Carrión, J. S., Fernández, S., González-Sampériz, P., Gil-Romera, G., Badal, E., Carrión-  
507 Marco, Y., López-Merino, L., López-Sáez, J. A., Fierro, E. and Burjachs, F.: Expected trends  
508 and surprises in the Lateglacial and Holocene vegetation history of the Iberian Peninsula and  
509 Balearic Islands, *Rev. Palaeobot. Palynol.*, 162(3), 458–475,  
510 doi:<https://doi.org/10.1016/j.revpalbo.2009.12.007>, 2010.
- 511 Carrión, Y., Kaal, J., López-Sáez, J. A., López-Merino, L. and Martínez Cortizas, A.:  
512 Holocene vegetation changes in NW Iberia revealed by anthracological and palynological  
513 records from a colluvial soil, *The Holocene*, 20(1), 53–66, doi:10.1177/0959683609348849,  
514 2009.



- 515 Carvalho, D., Pereira, S. and Rocha, A.: Future surface temperature changes for the Iberian  
 516 Peninsula according to EURO-CORDEX climate projections, *Clim. Dyn.*, 56, 1–16,  
 517 doi:10.1007/s00382-020-05472-3, 2021.
- 518 Cheddadi, R., Yu, G., Joel, G., Harrison, S., Prentice, I. and Colin, I.: The climate of Europe  
 519 6000 years ago, *cd*, 13, 1, doi:10.1007/s003820050148, 1997.
- 520 Chevalier, M., Davis, B. A. S., Heiri, O., Seppä, H., Chase, B. M., Gajewski, K., Lacourse,  
 521 T., Telford, R. J., Finsinger, W., Guiot, J., Köhl, N., Maezumi, S. Y., Tipton, J. R., Carter, V.  
 522 A., Brussel, T., Phelps, L. N., Dawson, A., Zanon, M., Vallé, F., Nolan, C., Mauri, A., de  
 523 Vernal, A., Izumi, K., Holmström, L., Marsicek, J., Goring, S., Sommer, P. S., Chaput, M.  
 524 and Kupriyanov, D.: Pollen-based climate reconstruction techniques for late Quaternary  
 525 studies, *Earth-Science Rev.*, 210, 103384,  
 526 doi:https://doi.org/10.1016/j.earscirev.2020.103384, 2020.
- 527 Connor, S., Vannièrè, B., Colombaroli, D., Anderson, R., Carrión, J., Ejarque, A., Gil-  
 528 Romera, G., Gonzalez Samperiz, P., Höfer, D., Morales-Molino, C., Revelles, J., Schneider,  
 529 H., Knaap, W., Leeuwen, J. and Woodbridge, J.: Humans take control of fire-driven diversity  
 530 changes in Mediterranean Iberia's vegetation during the mid-late Holocene, *The Holocene*,  
 531 29, 095968361982665, doi:10.1177/0959683619826652, 2019.
- 532 Cortés Sánchez, M., Jiménez Espejo, F. J., Simón Vallejo, M. D., Gibaja Bao, J. F., Carvalho,  
 533 A. F., Martínez-Ruiz, F., Gamiz, M. R., Flores, J.-A., Paytan, A., López Sáez, J. A., Peña-  
 534 Chocarro, L., Carrión, J. S., Morales Muñiz, A., Roselló Izquierdo, E., Riquelme Cantal, J.  
 535 A., Dean, R. M., Salgueiro, E., Martínez Sánchez, R. M., De la Rubia de Gracia, J. J., Lozano  
 536 Francisco, M. C., Vera Peláez, J. L., Rodríguez, L. L. and Bicho, N. F.: The Mesolithic–  
 537 Neolithic transition in southern Iberia, *Quat. Res.*, 77(2), 221–234,  
 538 doi:https://doi.org/10.1016/j.yqres.2011.12.003, 2012.
- 539 Dallmeyer, A., Claussen, M., Lorenz, S. J. and Shanahan, T.: The end of the African humid  
 540 period as seen by a transient comprehensive Earth system model simulation of the last 8000  
 541 years, , doi:10.5194/cp-2019-86, 2020.
- 542 Davis, B. A. S., Brewer, S., Stevenson, A. C. and Guiot, J.: The temperature of Europe during  
 543 the Holocene reconstructed from pollen data, *Quat. Sci. Rev.*, 22(15), 1701–1716,  
 544 doi:https://doi.org/10.1016/S0277-3791(03)00173-2, 2003.
- 545 Davis, T. W., Prentice, I. C., Stocker, B. D., Thomas, R. T., Whitley, R. J., Wang, H., Evans,  
 546 B. J., Gallego-Sala, A. V., Sykes, M. T. and Cramer, W.: Simple process-led algorithms for  
 547 simulating habitats (SPLASH v.1.0): Robust indices of radiation, evapotranspiration and  
 548 plant-available moisture, *Geosci. Model Dev.*, 10(2), 689–708, doi:10.5194/gmd-10-689-  
 549 2017, 2017.
- 550 Drake, B. L., Blanco-González, A. and Lillios, K. T.: Regional Demographic Dynamics in  
 551 the Neolithic Transition in Iberia: Results from Summed Calibrated Date Analysis, *J.*  
 552 *Archaeol. Method Theory*, 24(3), 796–812, doi:10.1007/s10816-016-9286-y, 2017.

- 553 Eilers, P. H. and Marx, B. D.: Practical smoothing: The Joys of P-splines, edited by P. H.  
554 Eilers and B. D. Marx, Cambridge University Press., 2021.
- 555 Farquhar, G. D.: Carbon dioxide and vegetation, *Science* (80-. ), 278(5342), 1411,  
556 doi:10.1126/science.278.5342.1411, 1997.
- 557 Fyfe, R. M., Woodbridge, J., Palmisano, A., Bevan, A., Shennan, S., Burjachs, F., Legarra  
558 Herrero, B., García Puchol, O., Carrión, J. S., Revelles, J. and Roberts, C. N.: Prehistoric  
559 palaeodemographics and regional land cover change in eastern Iberia, *Holocene*, 29(5), 799–  
560 815, doi:10.1177/0959683619826643, 2019.
- 561 García-Alix, A., Camuera, J., Ramos-Román, M. J., Toney, J. L., Sachse, D., Schefuß, E.,  
562 Jiménez-Moreno, G., Jiménez-Espejo, F. J., López-Avilés, A., Anderson, R. S. and Yanes,  
563 Y.: Paleohydrological dynamics in the Western Mediterranean during the last glacial cycle,  
564 *Glob. Planet. Change*, 202, 103527, doi:https://doi.org/10.1016/j.gloplacha.2021.103527,  
565 2021.
- 566 Gerhart, L. M. and Ward, J. K.: Plant responses to low [CO<sub>2</sub>] of the past, *New Phytol.*,  
567 188(3), 674–695, doi:https://doi.org/10.1111/j.1469-8137.2010.03441.x, 2010.
- 568 Githumbi, E., Fyfe, R., Gaillard, M.-J., Trondman, A.-K., Mazier, F., Nielsen, A.-B., Poska,  
569 A., Sugita, S., Woodbridge, J., Azuara, J., Feurdean, A., Grindean, R., Lebreton, V.,  
570 Marquer, L., Nebout-Combourieu, N., Stančikaitė, M., Tançuau, I., Tonkov, S.,  
571 Shumilovskikh, L. and data contributors, L.: European pollen-based REVEALS land-cover  
572 reconstructions for the Holocene: methodology, mapping and potentials, *Earth Syst. Sci.*  
573 *Data*, 14(4), 1581–1619, doi:10.5194/essd-14-1581-2022, 2022.
- 574 González-Sampériz, P., Aranbarri, J., Pérez-Sanz, A., Gil-Romera, G., Moreno, A., Leunda,  
575 M., Sevilla-Callejo, M., Corella, J. P., Morellón, M., Oliva, B. and Valero-Garcés, B.:  
576 Environmental and climate change in the southern Central Pyrenees since the Last Glacial  
577 Maximum: A view from the lake records, *Catena*, 149, 668–688,  
578 doi:https://doi.org/10.1016/j.catena.2016.07.041, 2017.
- 579 Granados, I. and Toro, M.: Recent warming in a high mountain lake (Laguna Cimera, Central  
580 Spain) inferred by means of fossil chironomids, *J. Limnol.*, 59 (suppl.), 109–119,  
581 doi:10.4081/jlimnol.2000.s1.109, 2000.
- 582 Hammer, O., Harper, D. and Ryan, P.: PAST: Paleontological statistics software package for  
583 education and data analysis, *Palaeontol. Electron.*, 4, 1–9, 2001.
- 584 Harrison, S., Shen, Y. and Sweeney, L.: Pollen data and charcoal data of the Iberian  
585 Peninsula (version 3), [online] Available from: <https://doi.org/10.17864/1947.000369>, 2022.
- 586 Harrison, S. P.: Modern pollen data for climate reconstructions, version 1 (SMPDS), ,  
587 doi:http://dx.doi.org/10.17864/1947.194, 2019.
- 588 Holden, P. B., Birks, H. J. B., Brooks, S. J., Bush, M. B., Hwang, G. M., Matthews-Bird, F.,

- 589 Valencia, B. G. and van Woesik, R.: BUMPER v1.0: a Bayesian user-friendly model for  
590 palaeo-environmental reconstruction, *Geosci. Model Dev.*, 10(1), 483–498,  
591 doi:10.5194/gmd-10-483-2017, 2017.
- 592 Ilvonen, L., López-Sáez, J. A., Holmström, L., Alba-Sánchez, F., Pérez-Díaz, S., Carrión, J.  
593 S., Ramos-Román, M. J., Camuera, J., Jiménez-Moreno, G., Ruha, L. and Seppä, H.: Spatial  
594 and temporal patterns of Holocene precipitation change in the Iberian Peninsula, *Boreas*,  
595 doi:https://doi.org/10.1111/bor.12586, 2022.
- 596 Kaufman, D., McKay, N., Routson, C., Erb, M., Davis, B., Heiri, O., Jaccard, S., Tierney, J.,  
597 Dätwyler, C., Axford, Y., Brussel, T., Cartapanis, O., Chase, B., Dawson, A., de Vernal, A.,  
598 Engels, S., Jonkers, L., Marsicek, J., Moffa-Sánchez, P., Morrill, C., Orsi, A., Rehfeld, K.,  
599 Saunders, K., Sommer, P. S., Thomas, E., Tonello, M., Tóth, M., Vachula, R., Andreev, A.,  
600 Bertrand, S., Biskaborn, B., Bringué, M., Brooks, S., Caniupán, M., Chevalier, M., Cwynar,  
601 L., Emile-Geay, J., Fegyveresi, J., Feurdean, A., Finsinger, W., Fortin, M.-C., Foster, L., Fox,  
602 M., Gajewski, K., Grosjean, M., Hausmann, S., Heinrichs, M., Holmes, N., Ilyashuk, B.,  
603 Ilyashuk, E., Juggins, S., Khider, D., Koinig, K., Langdon, P., Larocque-Tobler, I., Li, J.,  
604 Lotter, A., Luoto, T., Mackay, A., Magyari, E., Malevich, S., Mark, B., Massaferrro, J.,  
605 Montade, V., Nazarova, L., Novenko, E., Pařil, P., Pearson, E., Peros, M., Pienitz, R.,  
606 Płóciennik, M., Porinchu, D., Potito, A., Rees, A., Reinemann, S., Roberts, S., Rolland, N.,  
607 Salonen, S., Self, A., Seppä, H., Shala, S., St-Jacques, J.-M., Stenni, B., Syrykh, L., Tarrats,  
608 P., Taylor, K., van den Bos, V., Velle, G., Wahl, E., Walker, I., Wilmshurst, J., Zhang, E. and  
609 Zhilich, S.: A global database of Holocene paleotemperature records, *Sci. Data*, 7(1), 115,  
610 doi:10.1038/s41597-020-0445-3, 2020.
- 611 Liu, M., Prentice, I. C., ter Braak, C. J. F. and Harrison, S. P.: An improved statistical  
612 approach for reconstructing past climates from biotic assemblages, *Proc. R. Soc. A Math.*,  
613 476(2243), doi:https://doi.org/10.1098/rspa.2020.0346, 2020.
- 614 López-Merino, L., Cortizas, A. M. and López-Sáez, J. A.: Early agriculture and  
615 palaeoenvironmental history in the North of the Iberian Peninsula: a multi-proxy analysis of  
616 the Monte Areo mire (Asturias, Spain), *J. Archaeol. Sci.*, 37(8), 1978–1988,  
617 doi:https://doi.org/10.1016/j.jas.2010.03.003, 2010.
- 618 López-Sáez, J. A. and López-Merino, L.: Coprophilous fungi as a source of information of  
619 anthropic activities during the Prehistory in the Amblés Valley (Ávila, Spain): The  
620 archaeopalynological record, *Rev. Española Micropaleontol.*, 38, 49–75, 2007.
- 621 Martínez-Cortizas, A., Costa-Casais, M. and López-Sáez, J. A.: Environmental change in  
622 NW Iberia between 7000 and 500cal BC, *Quat. Int.*, 200(1), 77–89,  
623 doi:https://doi.org/10.1016/j.quaint.2008.07.012, 2009.
- 624 Mauri, A., Davis, B. A. S., Collins, P. M. and Kaplan, J. O.: The influence of atmospheric  
625 circulation on the mid-Holocene climate of Europe: a data–model comparison, *Clim. Past*,  
626 10(5), 1925–1938, doi:10.5194/cp-10-1925-2014, 2014.
- 627 Mauri, A., Davis, B. A. S., Collins, P. M. and Kaplan, J. O.: The climate of Europe during the  
628 Holocene: A gridded pollen-based reconstruction and its multi-proxy evaluation, *Quat. Sci.*

- 629 Rev., 112, 109–127, doi:10.1016/j.quascirev.2015.01.013, 2015.
- 630 Mighall, T. M., Martínez Cortizas, A., Biester, H. and Turner, S. E.: Proxy climate and  
631 vegetation changes during the last five millennia in NW Iberia: Pollen and non-pollen  
632 palynomorph data from two ombrotrophic peat bogs in the North Western Iberian Peninsula,  
633 Rev. Palaeobot. Palynol., 141(1–2), 203–223, doi:10.1016/j.revpalbo.2006.03.013, 2006.
- 634 Millet, L., Rius, D., Galop, D., Heiri, O. and Brooks, S. J.: Chironomid-based reconstruction  
635 of Lateglacial summer temperatures from the Ech palaeolake record (French western  
636 Pyrenees), Palaeogeogr. Palaeoclimatol. Palaeoecol., 315–316, 86–99,  
637 doi:https://doi.org/10.1016/j.palaeo.2011.11.014, 2012.
- 638 Morellón, M., Aranbarri, J., Moreno, A., González-Sampériz, P. and Valero-Garcés, B. L.:  
639 Early Holocene humidity patterns in the Iberian Peninsula reconstructed from lake, pollen  
640 and speleothem records, Quat. Sci. Rev., 181, 1–18,  
641 doi:https://doi.org/10.1016/j.quascirev.2017.11.016, 2018.
- 642 Muñoz Sobrino, C., Heiri, O., Hazekamp, M., van der Velden, D., Kirilova, E. P., García-  
643 Moreiras, I. and Lotter, A. F.: New data on the Lateglacial period of SW Europe: a high  
644 resolution multiproxy record from Laguna de la Roya (NW Iberia), Quat. Sci. Rev., 80, 58–  
645 77, doi:https://doi.org/10.1016/j.quascirev.2013.08.016, 2013.
- 646 New, M., Lister, D. and Hulme, M.: A high-resolution data set of surface climate over global  
647 land areas, Clim. Res., 21(1), 1–25 [online] Available from: [http://www.int-](http://www.int-res.com/abstracts/cr/v21/n1/p1-25/)  
648 [res.com/abstracts/cr/v21/n1/p1-25/](http://www.int-res.com/abstracts/cr/v21/n1/p1-25/), 2002.
- 649 Overpeck, J. T., Webb, T. and Prentice, I. C.: Quantitative interpretation of fossil pollen  
650 spectra: Dissimilarity coefficients and the method of modern analogs, Quat. Res., 23(1), 87–  
651 108, doi:10.1016/0033-5894(85)90074-2, 1985.
- 652 Parker, S. E., Harrison, S. P. and Braconnot, P.: Speleothem records of monsoon interannual-  
653 interdecadal variability through the Holocene, Environ. Res. Commun., 3(12), 121002,  
654 doi:10.1088/2515-7620/ac3eaa, 2021.
- 655 Peña-Chocarro, L., Peña, L. Z., Gazólaz, J. G., Morales, M. G., Sesma, J. S. and Straus, L.  
656 G.: The spread of agriculture in northern Iberia: new archaeobotanical data from El Mirón  
657 cave (Cantabria) and the open-air site of Los Cascajos (Navarra), Veg. Hist. Archaeobot.,  
658 14(4), 268–278, doi:10.1007/s00334-005-0078-7, 2005.
- 659 Peyron, O., Guiot, J., Cheddadi, R., Tarasov, P., Reille, M., de Beaulieu, J.-L., Bottema, S.  
660 and Andrieu, V.: Climatic reconstruction in Europe for 18,000 yr B.P. from pollen data, Quat.  
661 Res., 49(2), 183–196, doi:https://doi.org/10.1006/qres.1997.1961, 1998.
- 662 Prentice, I. C. and Harrison, S. P.: Ecosystem effects of CO<sub>2</sub> concentration: evidence from  
663 past climates, Clim. Past, 5(3), 297–307, doi:10.5194/cp-5-297-2009, 2009.
- 664 Prentice, I. C., Meng, T., Wang, H., Harrison, S. P., Ni, J. and Wang, G.: Evidence of a

- 665 universal scaling relationship for leaf CO<sub>2</sub> drawdown along an aridity gradient, *New Phytol.*,  
666 190(1), 169–180, doi:<https://doi.org/10.1111/j.1469-8137.2010.03579.x>, 2011.
- 667 Prentice, I. C., Cleator, S. F., Huang, Y. H., Harrison, S. P. and Roulstone, I.: Reconstructing  
668 ice-age palaeoclimates: Quantifying low-CO<sub>2</sub> effects on plants, *Glob. Planet. Change*, 149,  
669 166–176, doi:<https://doi.org/10.1016/j.gloplacha.2016.12.012>, 2017.
- 670 Prentice, I. C., Villegas-Diaz, R. and Harrison, S. P.: Accounting for atmospheric carbon  
671 dioxide variations in pollen-based reconstruction of past hydroclimates, *Glob. Planet.*  
672 *Change*, 2022.
- 673 Ramos-Román, M. J., Jiménez-Moreno, G., Camuera, J., García-Alix, A., Anderson, R.,  
674 Jiménez-Espejo, F., Sachse, D., Jaime, T., Carrión, J., Webster, C. and Yanes, Y.: Millennial-  
675 scale cyclical environment and climate variability during the Holocene in the western  
676 Mediterranean region deduced from a new multi-proxy analysis from the Padul record (Sierra  
677 Nevada, Spain), *Glob. Planet. Change*, 168, doi:[10.1016/j.gloplacha.2018.06.003](https://doi.org/10.1016/j.gloplacha.2018.06.003), 2018.
- 678 Reimer, P. J., Austin, W. E. N., Bard, E., Bayliss, A., Blackwell, P. G., Bronk Ramsey, C.,  
679 Butzin, M., Cheng, H., Edwards, R. L., Friedrich, M., Grootes, P. M., Guilderson, T. P.,  
680 Hajdas, I., Heaton, T. J., Hogg, A. G., Hughen, K. A., Kromer, B., Manning, S. W.,  
681 Muscheler, R., Palmer, J. G., Pearson, C., Van Der Plicht, J., Reimer, R. W., Richards, D. A.,  
682 Scott, E. M., Southon, J. R., Turney, C. S. M., Wacker, L., Adolphi, F., Büntgen, U., Capano,  
683 M., Fahrni, S. M., Fogtmann-Schulz, A., Friedrich, R., Köhler, P., Kudsk, S., Miyake, F.,  
684 Olsen, J., Reinig, F., Sakamoto, M., Sookdeo, A. and Talamo, S.: The IntCal20 Northern  
685 Hemisphere radiocarbon age calibration curve (0-55 cal kBP), *Radiocarbon*, 62(4), 725–757,  
686 doi:[10.1017/RDC.2020.41](https://doi.org/10.1017/RDC.2020.41), 2020.
- 687 Revelles, J., Burjachs, F., Palomo, A., Piqué, R., Iriarte, E., Pérez-Obiol, R. and Terradas, X.:  
688 Human-environment interaction during the Mesolithic- Neolithic transition in the NE Iberian  
689 Peninsula. Vegetation history, climate change and human impact during the Early-Middle  
690 Holocene in the Eastern Pre-Pyrenees, *Quat. Sci. Rev.*, 184, 183–200,  
691 doi:<https://doi.org/10.1016/j.quascirev.2017.08.025>, 2018.
- 692 Salonen, J. S., Ilvonen, L., Seppä, H., Holmström, L., Telford, R. J., Gaidamavičius, A.,  
693 Stančikaitė, M. and Subetto, D.: Comparing different calibration methods (WA/WA-PLS  
694 regression and Bayesian modelling) and different-sized calibration sets in pollen-based  
695 quantitative climate reconstruction, *The Holocene*, 22(4), 413–424,  
696 doi:[10.1177/0959683611425548](https://doi.org/10.1177/0959683611425548), 2011.
- 697 Salonen, J. S., Korpela, M., Williams, J. W. and Luoto, M.: Machine-learning based  
698 reconstructions of primary and secondary climate variables from North American and  
699 European fossil pollen data, *Sci. Rep.*, 9(1), 15805, doi:[10.1038/s41598-019-52293-4](https://doi.org/10.1038/s41598-019-52293-4), 2019.
- 700 Schröder, T., López-Sáez, J. A., van't Hoff, J. and Reicherter, K.: Unravelling the Holocene  
701 environmental history of south-western Iberia through a palynological study of Lake Medina  
702 sediments, *The Holocene*, 30(1), 13–22, doi:[10.1177/0959683619865590](https://doi.org/10.1177/0959683619865590), 2019.

- 703 Shen, Y., Sweeney, L., Liu, M., Lopez Saez, J. A., Pérez-Díaz, S., Luelmo-Lautenschlaeger,  
704 R., Gil-Romera, G., Hofer, D., Jiménez-Moreno, G., Schneider, H., Prentice, I. C. and  
705 Harrison, S. P.: Reconstructing burnt area during the Holocene: an Iberian case study, *Clim.*  
706 *Past*, 18, 1189–1201, doi:10.5194/cp-2021-36, 2022.
- 707 Stoll, H. M., Moreno, A., Mendez-Vicente, A., Gonzalez-Lemos, S., Jimenez-Sanchez, M.,  
708 Dominguez-Cuesta, M. J., Edwards, R. L., Cheng, H. and Wang, X.: Paleoclimate and  
709 growth rates of speleothems in the northwestern Iberian Peninsula over the last two glacial  
710 cycles, *Quat. Res.*, 80, 284–290, doi:10.1016/j.yqres.2013.05.002, 2013.
- 711 Tarrats, P., Heiri, O., Valero-Garcés, B., Cañedo-Argüelles, M., Prat, N., Rieradevall, M. and  
712 González-Sampériz, P.: Chironomid-inferred Holocene temperature reconstruction in Basa de  
713 la Mora Lake (Central Pyrenees), *The Holocene*, 28(11), 1685–1696,  
714 doi:10.1177/0959683618788662, 2018.
- 715 Tarroso, P., Carrión, J., Dorado-Valiño, M., Queiroz, P., Santos, L., Valdeolillos-  
716 Rodríguez, A., Célio Alves, P., Brito, J. C. and Cheddadi, R.: Spatial climate dynamics in the  
717 Iberian Peninsula since 15 000 yr BP, *Clim. Past*, 12(5), 1137–1149, doi:10.5194/cp-12-  
718 1137-2016, 2016.
- 719 Thatcher, D. L., Wanamaker, A. D., Denniston, R. F., Asmerom, Y., Polyak, V. J., Fullick,  
720 D., Ummenhofer, C. C., Gillikin, D. P. and Haws, J. A.: Hydroclimate variability from  
721 western Iberia (Portugal) during the Holocene: Insights from a composite stalagmite isotope  
722 record, *The Holocene*, 30(7), 966–981, doi:https://doi.org/10.1177/0959683620908648,  
723 2020.
- 724 Trondman, A.-K., Gaillard, M.-J., Mazier, F., Sugita, S., Fyfe, R., Nielsen, A. B., Twiddle,  
725 C., Barratt, P., Birks, H. J. B., Bjune, A. E., Björkman, L., Broström, A., Caseldine, C.,  
726 David, R., Dodson, J., Dörfler, W., Fischer, E., van Geel, B., Giesecke, T., Hultberg, T.,  
727 Kalnina, L., Kangur, M., van der Knaap, P., Koff, T., Kuneš, P., Lagerås, P., Latałowa, M.,  
728 Lechterbeck, J., Leroyer, C., Leydet, M., Lindbladh, M., Marquer, L., Mitchell, F. J. G.,  
729 Odgaard, B. V., Peglar, S. M., Persson, T., Poska, A., Rösch, M., Seppä, H., Veski, S. and  
730 Wick, L.: Pollen-based quantitative reconstructions of Holocene regional vegetation cover  
731 (plant-functional types and land-cover types) in Europe suitable for climate modelling, *Glob.*  
732 *Chang. Biol.*, 21(2), 676–697, doi:https://doi.org/10.1111/gcb.12737, 2015.
- 733 Villegas-Diaz, Roberto; Cruz-Silva, Esmeralda; Harrison, S. P.: ageR: Supervised age  
734 models, , doi:10.5281/zenodo.4636715, 2021.
- 735 Walczak, I. W., Baldini, J. U. L., Baldini, L. M., McDermott, F., Marsden, S., Standish, C.  
736 D., Richards, D. A., Andreo, B. and Slater, J.: Reconstructing high-resolution climate using  
737 CT scanning of unsectioned stalagmites: A case study identifying the mid-Holocene onset of  
738 the Mediterranean climate in southern Iberia, *Quat. Sci. Rev.*, 127, 117–128,  
739 doi:https://doi.org/10.1016/j.quascirev.2015.06.013, 2015.
- 740 Wei, D., González-Sampériz, P., Gil-Romera, G., Harrison, S. P. and Prentice, I. C.: Seasonal  
741 temperature and moisture changes in interior semi-arid Spain from the last interglacial to the  
742 Late Holocene, *Quat. Res.*, 101, 143–155, doi:DOI: 10.1017/qua.2020.108, 2021.

- 743 Wu, H., Guiot, J., Brewer, S. and Guo, Z.: Climatic changes in Eurasia and Africa at the last  
744 glacial maximum and mid-Holocene: reconstruction from pollen data using inverse  
745 vegetation modelling, *Clim. Dyn.*, 29(2), 211–229, doi:10.1007/s00382-007-0231-3, 2007.
- 746 Zapata, L., Peña-Chocarro, L., Pérez-Jordá, G. and Stika, H.-P.: Early Neolithic Agriculture  
747 in the Iberian Peninsula, *J. World Prehistory*, 18(4), 283–325 [online] Available from:  
748 <http://www.jstor.org/stable/25801225>, 2004.
- 749

## 750 **Figure and Table Captions**

751 Figure 1. Climate space represented by mean temperature of the coldest month (MTCO),  
 752 mean temperature of the warmest month (MTWA), and plant-available moisture as  
 753 represented by  $\alpha$ , an estimate of the ratio of actual evapotranspiration to equilibrium  
 754 evapotranspiration. The grey points show climate values for a rectangular area (21° W ~ 150°  
 755 E, 29° N ~ 82° N) enclosing the SMPDS data set, derived from the Climate Research Unit  
 756 CRU CL 2.0 database (New et al., 2002). The black points show climate values of the  
 757 SMPDS dataset. The red points show climate values of the Iberian Peninsula region in the  
 758 SMPDS dataset.

759 Figure 2. Map showing the location of the 117 fossil sites in the Iberian Peninsula used for  
 760 climate reconstructions. Sites lower than 1000 m a.s.l. are shown as squares, sites higher than  
 761 1000 m a.s.l. are shown as triangles. The base maps show modern (a) mean temperature of  
 762 the coldest month (MTCO), (b) mean temperature of the warmest month (MTWA), and (c)  
 763 plant-available moisture as represented by  $\alpha$ , an estimate of the ratio of actual  
 764 evapotranspiration to equilibrium evapotranspiration.

765 Figure 3. Reconstructed anomalies in climate at individual sites through time. The sites are  
 766 grouped into high (>1000m) and low (<1000m) elevation sites and organised from west to east.  
 767 Grey cells indicate periods or longitudes with no data. The individual plots show the anomalies  
 768 in reconstructed (a,d) mean temperature of the coldest month (MTCO), (b,e) mean temperature  
 769 of the warmest month (MTWA), and (c,f) plant-available moisture as represented by  $\alpha$ , an  
 770 estimate of the ratio of actual evapotranspiration to equilibrium evapotranspiration. The  
 771 anomalies are expressed as deviations of the mean value in each bin ( $\pm 500$  years) from the  
 772 value at 0.5 ka at each site.

773 Figure 4. Reconstructed composite changes (anomalies to 0.5 ka) in (a) mean temperature of  
 774 the coldest month (MTCO), (b) mean temperature of the warmest month (MTWA) and (c)  
 775 plant-available moisture as represented by  $\alpha$ , through the Holocene compared to changes in  
 776 (d) winter and (e) summer insolation for the latitude of the Iberian Peninsula, using  $\pm 500$   
 777 years as the bin. The black lines show mean values across sites, with vertical line segments  
 778 showing the standard deviations of mean values using 1000 bootstrap cycles of site  
 779 resampling.

780 Figure 5. Changes in the west-east gradient of plant-available moisture as represented by  
 781 anomalies in  $\alpha$  relative to 0.5 ka at individual sites through the Holocene. The red lines show  
 782 the regression lines. The shades indicate the 95 % confidence intervals of the regression lines



783 Figure 6. The relationship between mean temperature of the warmest month (MTWA) and  
 784 plant-available moisture as represented by  $\alpha$  (a) in the modern climate data set, and (b) in the  
 785 Holocene reconstructions.

786 Figure 7. Comparison between reconstructed composite changes in climate anomalies. The first  
 787 column represents this paper, the second column represents Mauri et al. (2015), the third  
 788 column represents Kaufman et al. (2020), the fourth column represents Tarroso et al. (2016).  
 789 The composite curves from this paper and Kaufman et al. (2020) are calculated from individual  
 790 reconstructions, using anomalies to 0.5 ka and a bin of  $\pm 500$  years (time slices are 0.5, 1.5, ...,  
 791 11.5 ka). The composite curves from Mauri et al. (2015) are converted directly from the gridded  
 792 time slices which are provided with anomalies to 0.1 ka and a bin of  $\pm 500$  years (time slices  
 793 are 1, 2, ..., 12 ka). The composite curves from Tarroso et al. (2016) are also converted directly  
 794 from the gridded time slices provided, with anomalies to 0.5 ka and a bin of  $\pm 500$  years (time  
 795 slices are 3, 4, ..., 12 ka). Note that Tarroso et al. (2016) applied a smoothing to the data such  
 796 that the plots in the paper do not show the excursion in MTWA at 8 ka. In all of the plots, the  
 797 black lines show mean values across sites, with vertical line bars showing the standard  
 798 deviation of mean values using 1000 bootstrap cycles of site/grid resampling.

799 Figure 8. Simulated mean values of mean temperature of the coldest month (MTCO), mean  
 800 temperature of the warmest month (MTWA) and mean daily precipitation in Iberian Peninsula  
 801 between 8 ka and 0 ka, smoothed using 100 year bins. Here BP means before 1950 AD. The  
 802 black lines represent Max Planck Institute Earth System Model (MPI) simulations, the red lines  
 803 represent Alfred Wagner Insitute Earth System Model (AWI) simulations, the blue lines  
 804 represent Institut Pierre Simon Laplace Climate Model (IPSL-CM5) TR5AS simulations, the  
 805 orange lines represent Institut Pierre Simon Laplace Climate Model (IPSL-CM6) TR6AV  
 806 simulations. The four simulations were forced by evolving orbital parameters and greenhouse  
 807 gas concentrations. The four models have different spatial resolution, with the finest resolution  
 808 being  $1.875^\circ \times 1.875^\circ$  (AWI, MPI) and the coarsest resolution being  $1.875^\circ \times 3.75^\circ$  (IPSL-  
 809 CM5, TR5AS).

810 Table 1. Details of the fossil pollen sites used. The fossil pollen data from the Iberian  
 811 Peninsula were compiled by Shen et al. (2021) and obtained from  
 812 <https://doi.org/10.17864/1947.000343>. The reference list of this table can be found in the  
 813 supplementary.

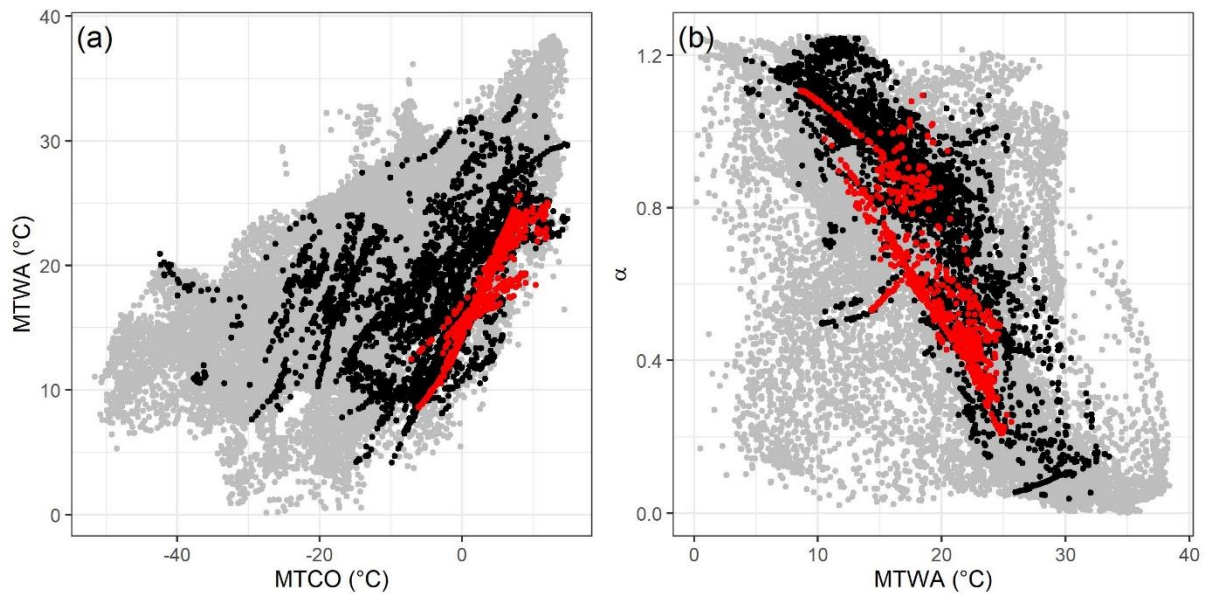
814 Table 2. Leave-out cross-validation (with geographically and climatically close sites  
 815 removed) fitness of the modified version of fxTWA-PLS, for mean temperature of the coldest  
 816 month (MTCO), mean temperature of the warmest month (MTWA) and plant-available  
 817 moisture ( $\alpha$ ), with p-spline smoothed fx estimation, using bins of 0.02, 0.02 and 0.002,  
 818 showing results for all the components. RMSEP is the root-mean-square error of prediction.

819  $\Delta$ RMSEP is the per cent change of RMSEP using the current number of components than  
820 using one component less.  $p$  assesses whether using the current number of components is  
821 significantly different from using one component less, which is used to choose the last  
822 significant number of components (indicated in bold) to avoid over-fitting. The degree of  
823 overall compression is assessed by linear regression of the cross-validated reconstructions  
824 onto the climate variable,  $b_1$ ,  $b_1.se$  are the slope and the standard error of the slope,  
825 respectively. The closer the slope ( $b_1$ ) is to 1, the less the overall compression is.

826 Table 3. Canonical Correspondence Analysis (CCA) result of modern and fossil-  
827 reconstructed MTCO, MTWA and  $\alpha$ . The summary statistics for the ANOVA-like  
828 permutation test (999 permutations) are also shown. VIF is the variance inflation factor, Df is  
829 the number of degrees of freedom,  $\chi^2$  is the constrained eigenvalue (or the sum of constrained  
830 eigenvalues for the whole model), F is significance, and Pr ( $>F$ ) is the probability. The CCA  
831 plots can be found in the Supplementary (Fig. S11).

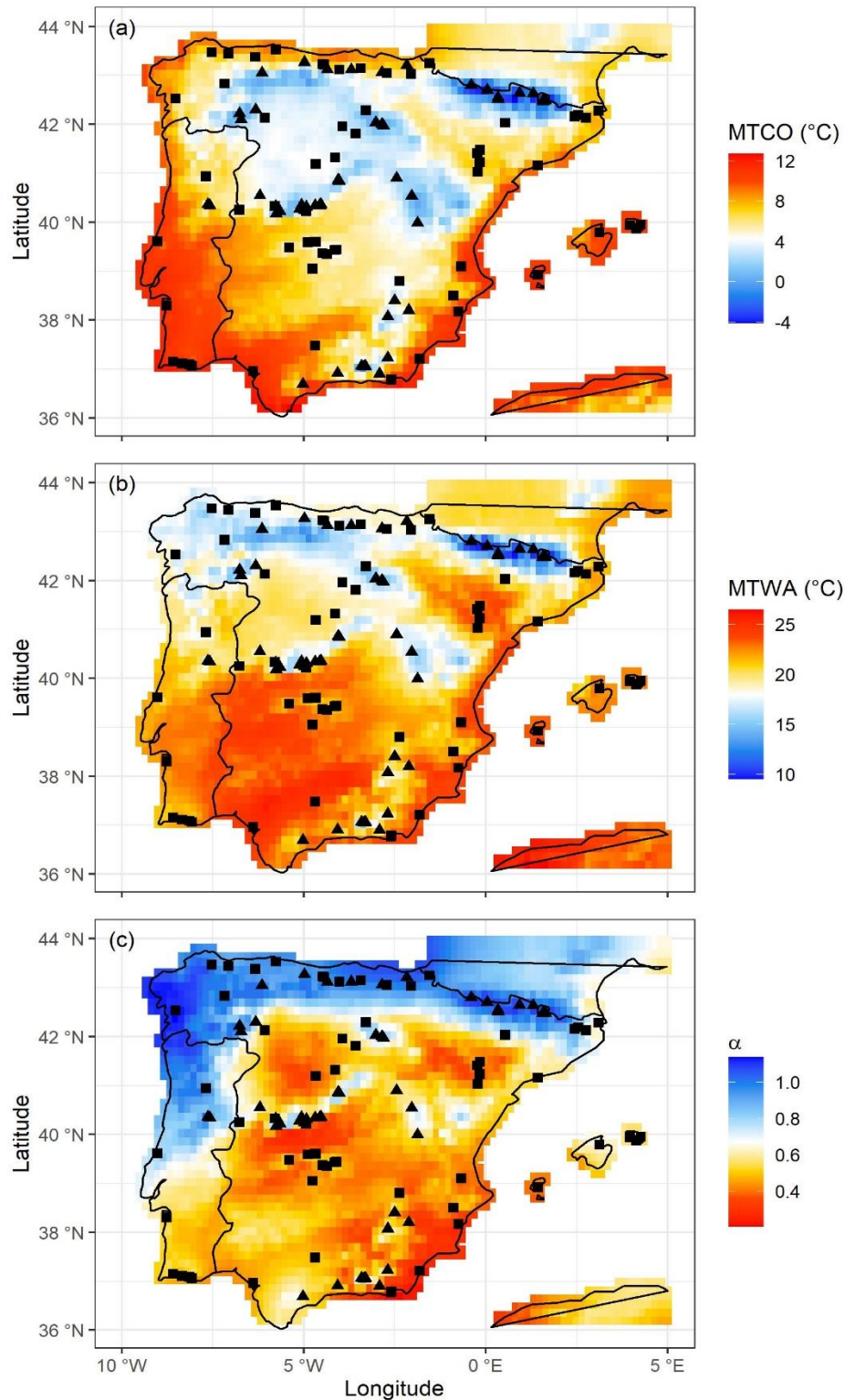
832 Table 4. Assessment of the significance of anomalies to 0.5 ka through time with latitude and  
833 elevation. The slope is obtained by linear regression of the anomaly onto the longitude or  
834 elevation.  $p$  is the significance of the slope (bold parts:  $p < 0.05$ ).  $x_0$  is the point where the  
835 anomaly is 0 in the linear equation, which indicates longitude or elevation where the anomaly  
836 changes sign.

837 Figure 1. Climate space represented by mean temperature of the coldest month (MTCO),  
838 mean temperature of the warmest month (MTWA), and plant-available moisture as  
839 represented by  $\alpha$ , an estimate of the ratio of actual evapotranspiration to equilibrium  
840 evapotranspiration. The grey points show climate values for a rectangular area (21° W ~ 150°  
841 E, 29° N ~ 82° N) enclosing the SMPDS data set, derived from the Climate Research Unit  
842 CRU CL 2.0 database (New et al., 2002). The black points show climate values of the  
843 SMPDS dataset. The red points show climate values of the Iberian Peninsula region in the  
844 SMPDS dataset.  
845



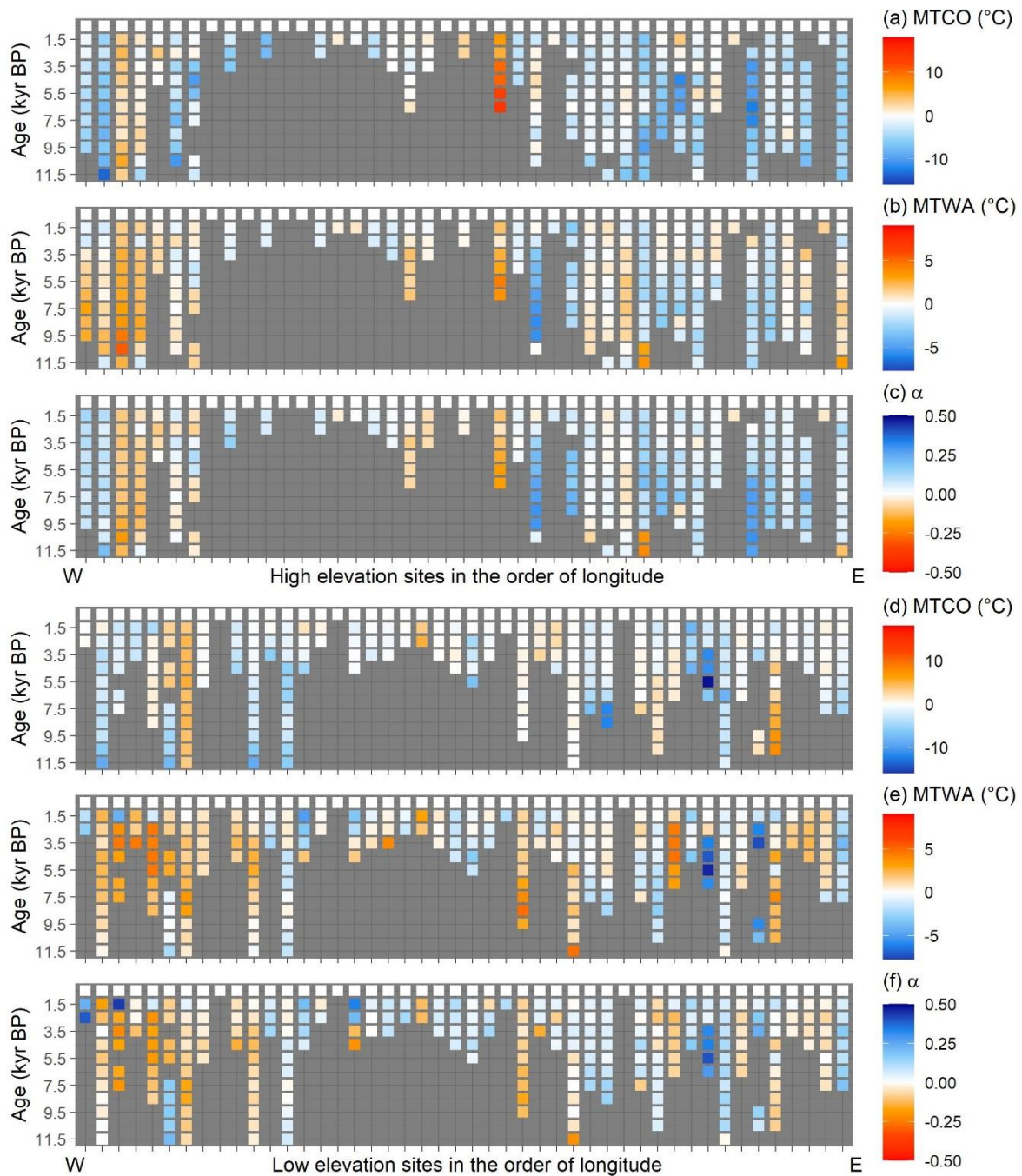
846

847 Figure 2. Map showing the location of the 117 fossil sites in the Iberian Peninsula used for  
 848 climate reconstructions. Sites lower than 1000 m a.s.l. are shown as squares, sites higher than  
 849 1000 m a.s.l. are shown as triangles. The base maps show modern (a) mean temperature of the  
 850 coldest month (MTCO), (b) mean temperature of the warmest month (MTWA), and (c)  
 851 plant-available moisture as represented by  $\alpha$ , an estimate of the ratio of actual  
 852 evapotranspiration to equilibrium evapotranspiration.  
 853



854

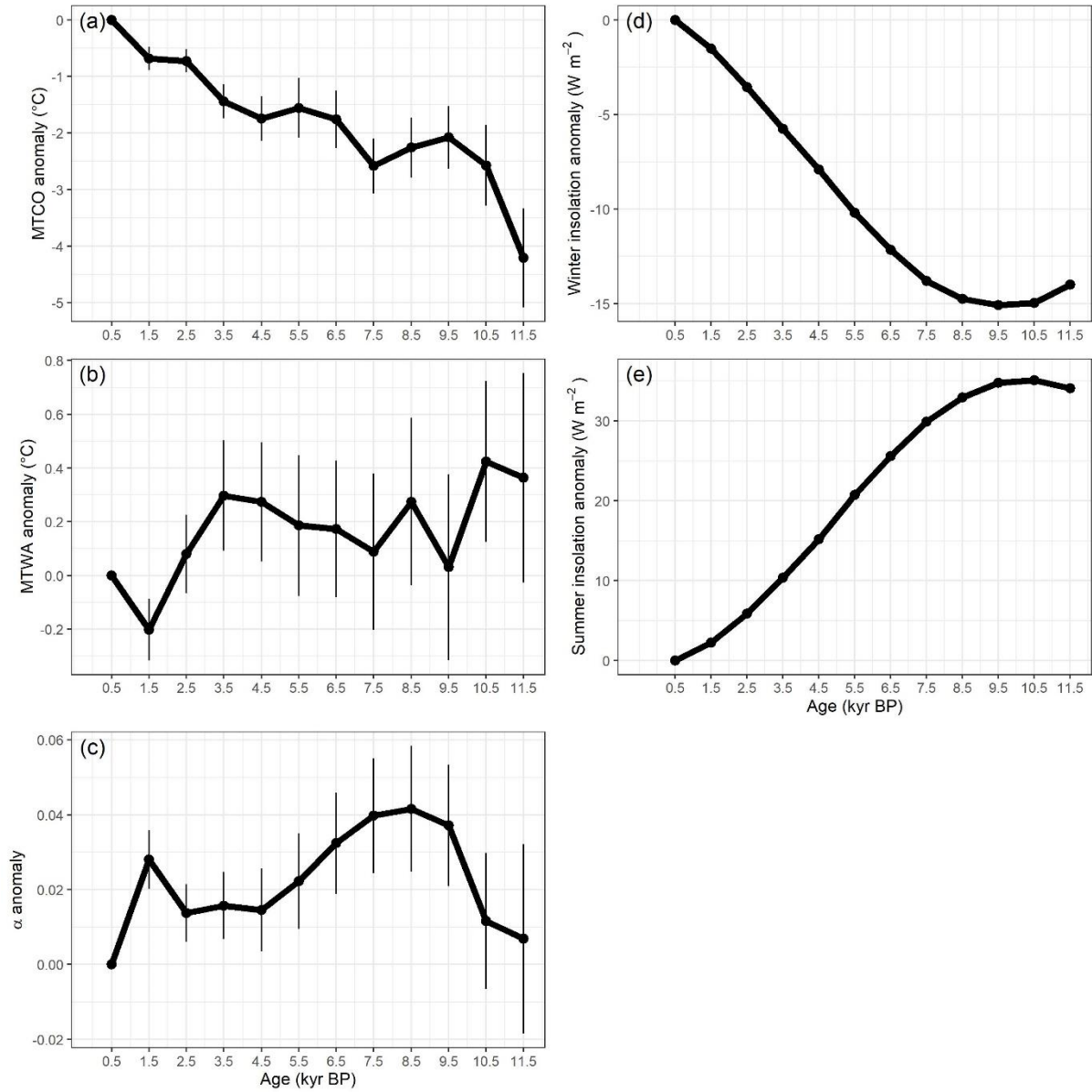
855 Figure 3. Reconstructed anomalies in climate at individual sites through time. The sites are  
 856 grouped into high (>1000m) and low (<1000m) elevation sites and organised from west to  
 857 east. Grey cells indicate periods or longitudes with no data. The individual plots show the  
 858 anomalies in reconstructed (a,d) mean temperature of the coldest month (MTCO), (b,e) mean  
 859 temperature of the warmest month (MTWA), and (c,f) plant-available moisture as  
 860 represented by  $\alpha$ , an estimate of the ratio of actual evapotranspiration to equilibrium  
 861 evapotranspiration. The anomalies are expressed as deviations of the mean value in each bin  
 862 ( $\pm 500$  years) from the value at 0.5 ka at each site.  
 863



864

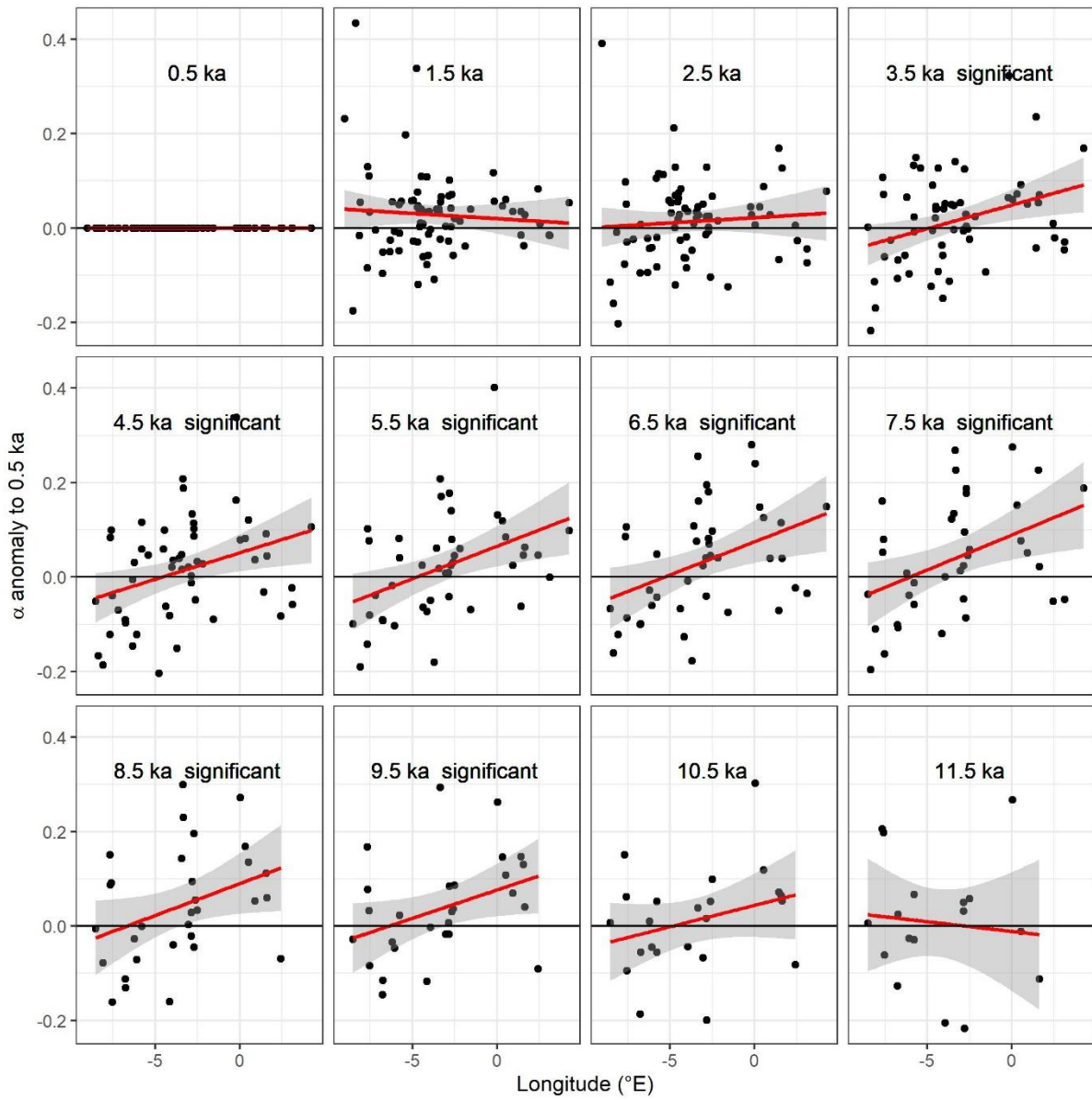


865 Figure 4. Reconstructed composite changes (anomalies to 0.5 ka) in (a) mean temperature of  
 866 the coldest month (MTCO), (b) mean temperature of the warmest month (MTWA) and (c)  
 867 plant-available moisture as represented by  $\alpha$ , through the Holocene compared to changes in  
 868 (d) winter and (e) summer insolation for the latitude of the Iberian Peninsula, using  $\pm 500$   
 869 years as the bin. The black lines show mean values across sites, with vertical line segments  
 870 showing the standard deviations of mean values using 1000 bootstrap cycles of site  
 871 resampling.  
 872



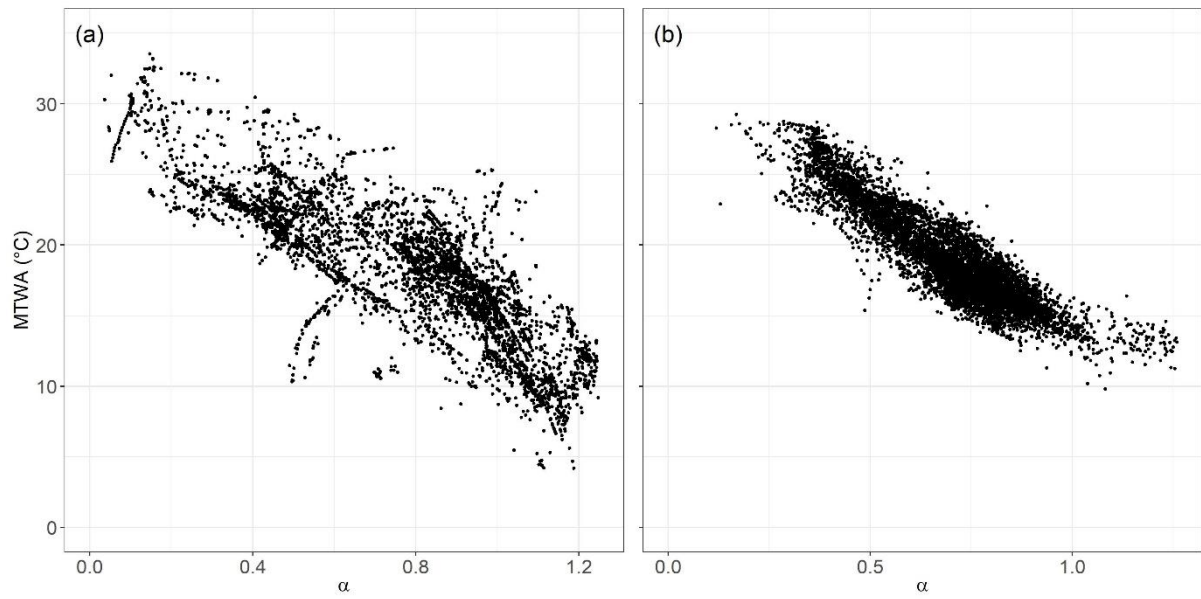
873

874 Figure 5. Changes in the west-east gradient of plant-available moisture as represented by  
 875 anomalies in  $\alpha$  relative to 0.5 ka at individual sites through the Holocene. The red lines show  
 876 the regression lines. The shades indicate the 95 % confidence intervals of the regression lines.  
 877



878

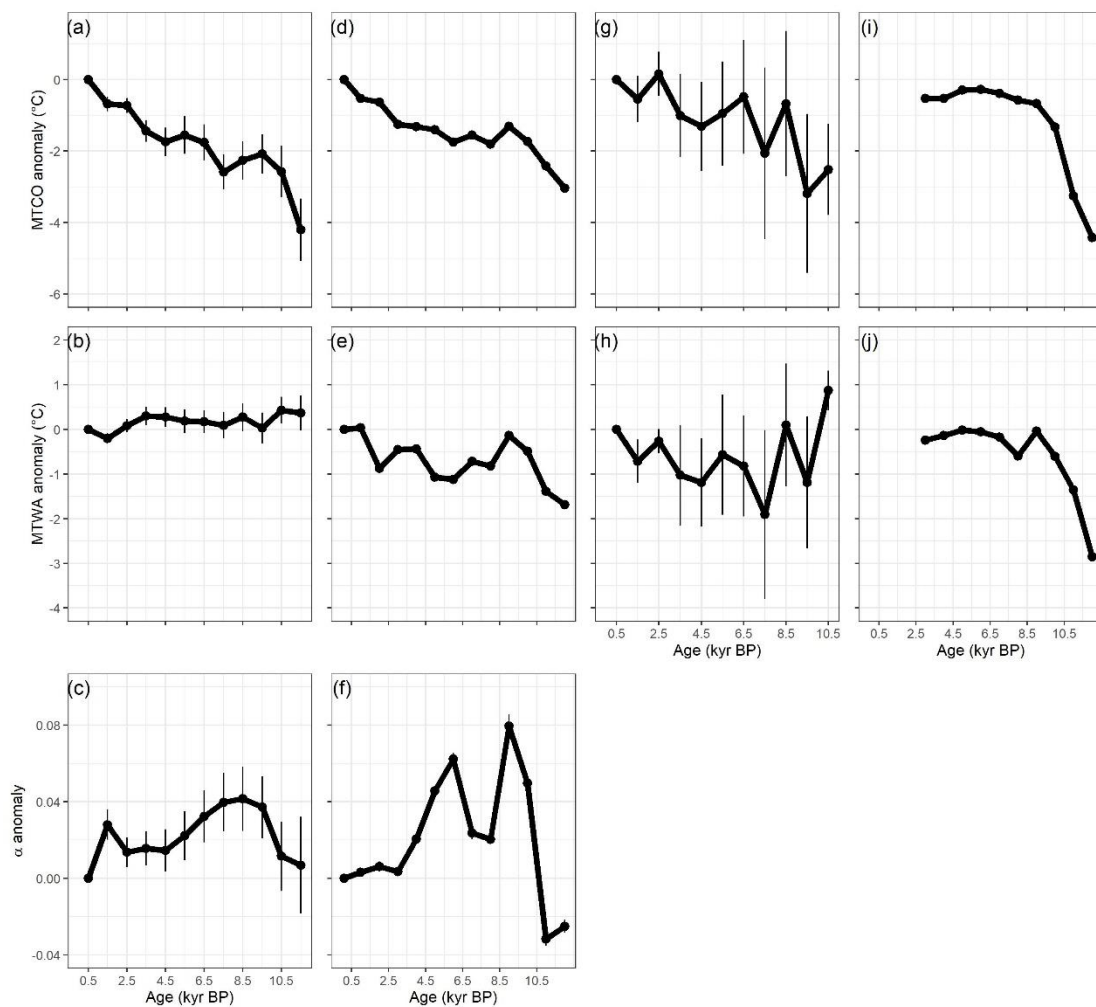
879 Figure 6. The relationship between mean temperature of the warmest month (MTWA) and  
880 plant-available moisture as represented by  $\alpha$  (a) in the modern climate data set, and (b) in the  
881 Holocene reconstructions.  
882



883  
884  
885

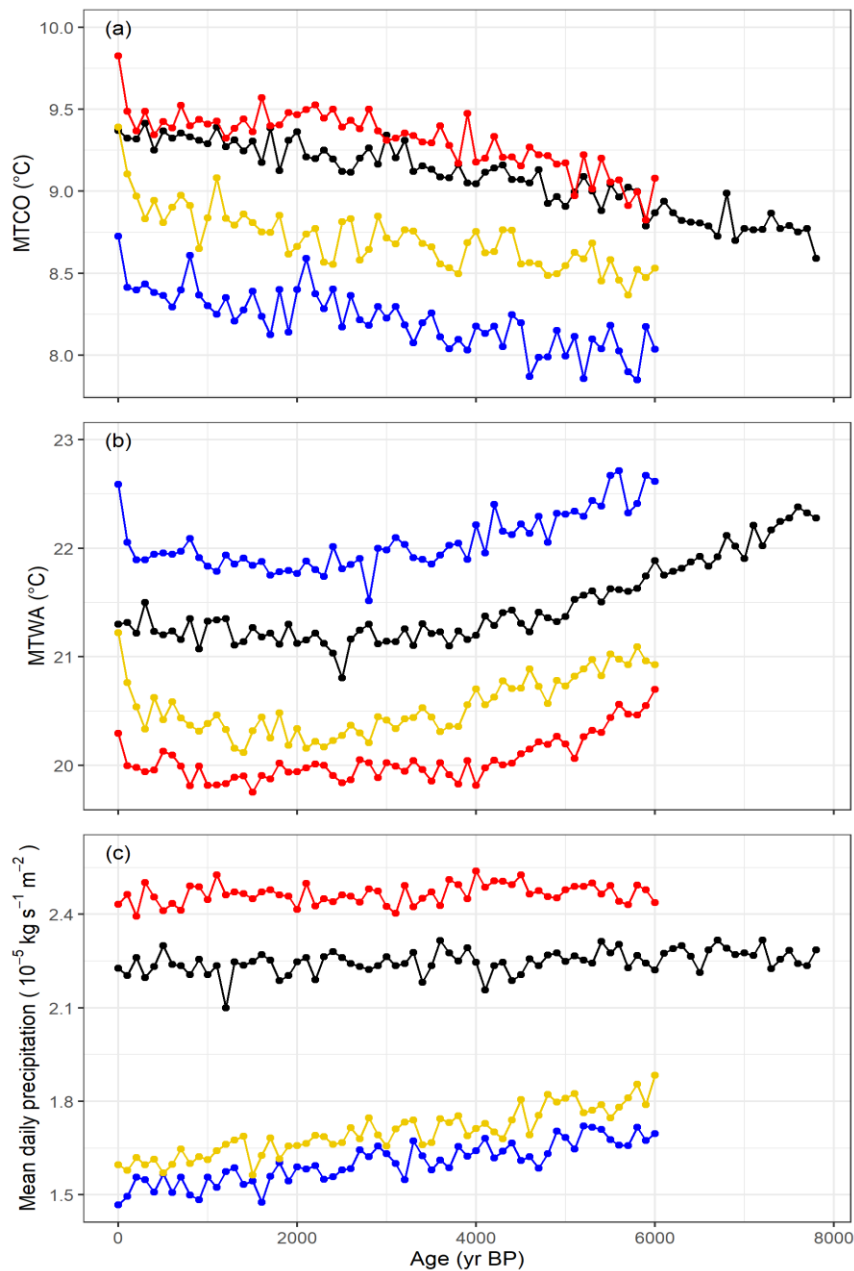


886 Figure 7. Comparison between reconstructed composite changes in climate anomalies. The first  
 887 column represents this paper, the second column represents Mauri et al. (2015), the third  
 888 column represents Kaufman et al. (2020), the fourth column represents Tarroso et al. (2016).  
 889 The composite curves from this paper and Kaufman et al. (2020) are calculated from individual  
 890 reconstructions, using anomalies to 0.5 ka and a bin of  $\pm 500$  years (time slices are 0.5, 1.5, ...,  
 891 11.5 ka). The composite curves from Mauri et al. (2015) are converted directly from the gridded  
 892 time slices which are provided with anomalies to 0.1 ka and a bin of  $\pm 500$  years (time slices  
 893 are 1, 2, ..., 12 ka). The composite curves from Tarroso et al. (2016) are also converted directly  
 894 from the gridded time slices provided, with anomalies to 0.5 ka and a bin of  $\pm 500$  years (time  
 895 slices are 3, 4, ..., 12 ka). Note that Tarroso et al. (2016) applied a smoothing to the data such  
 896 that the plots in the paper do not show the excursion in MTWA at 8 ka. In all of the plots, the  
 897 black lines show mean values across sites, with vertical line bars showing the standard  
 898 deviation of mean values using 1000 bootstrap cycles of site/grid resampling.  
 899



900  
 901

902 Figure 8. Simulated mean values of mean temperature of the coldest month (MTCO), mean  
 903 temperature of the warmest month (MTWA) and mean daily precipitation in Iberian  
 904 Peninsula between 8 ka and 0 ka, smoothed using 100 year bins. Here BP means before 1950  
 905 AD. The black lines represent Max Planck Institute Earth System Model (MPI) simulations,  
 906 the red lines represent Alfred Wagner Insitute Earth System Model (AWI) simulations, the  
 907 blue lines represent Institut Pierre Simon Laplace Climate Model (IPSL-CM5) TR5AS  
 908 simulations, the orange lines represent Institut Pierre Simon Laplace Climate Model (IPSL-  
 909 CM6) TR6AV simulations. The four simulations were forced by evolving orbital parameters  
 910 and greenhouse gas concentrations. The four models have different spatial resolution, with  
 911 the finest resolution being  $1.875^\circ \times 1.875^\circ$  (AWI, MPI) and the coarsest resolution being  
 912  $1.875^\circ \times 3.75^\circ$  (IPSL-CM5, TR5AS).



913

914 Table 1. Details of the fossil pollen sites used. The fossil pollen data from the Iberian Peninsula were compiled by Shen et al. (2021) and obtained  
 915 from <https://doi.org/10.17864/1947.000343>. The reference list of this table can be found in the supplementary.  
 916

site name	entity name	longitudo (°E)	latitude (°N)	elevation (m)	earliest sample (yr BP)	latest sample (yr BP)	length of record (yr)	no of samples	no of dating points	source	reference
Albufera Alcudia	ALCUDIA	3.12	39.79	0	7921	17	7904	54	4	EPD	Burjachs et al., (1994)
Algendar	ALGENDAR	3.96	39.94	21	8908	3816	5092	118	4	EPD	Yll et al., (1995, 1997)
Almenara de Adaja	ADAJA	-4.67	41.19	784	2830	477	2353	25	2	EPD	López Merino et al., (2009)
Alsa	ALSA	-4.02	43.12	560	4908	150	4758	24	3	EPD	Mariscal (1993)
Alvor Estuary Ribeira do Farelo Ribeira da Torre	Abi 05/07	-8.59	37.15	1	7840	1699	6141	76	9	author	Schneider et al., (2010, 2016)
Antas	ANTAS	-1.82	37.21	0	11141	4309	6832	95	6	EPD	Yll et al., (1995); Cano Villanueva, J. P. (1997); Pantaléon-Cano et al., (2003)
Arbarrain Mire	ARBARRAIN	-2.17	43.21	1004	6872	78	6794	91	8	author	Pérez-Díaz et al., (2018)
Armacao de Pera Ribeira de Alcantarilha	ADP 01/06	-8.34	37.11	2	7926	8	7918	17	7	author	Schneider et al., (2010, 2016)
Armena	Armena	0.34	42.51	2238	5668	2217	3451	53	27	author	Leunda et al., (2019)
Arroyo de Aguas Frias	AGUASFRIAS	-5.12	40.27	1120	196	-41	237	50	5	author	Julio Camarero et al., (2019)
Arroyo de las Cárcavas	CARCAVAS	-4.03	40.84	1300	2346	-57	2403	40	6	EPD	Morales-Molino et al., (2017a)
Arroyo de Navalacarreta	NAVALACA	-4.03	40.85	1250	706	-60	766	38	6	EPD	Morales-Molino et al., (2017a)
Arroyo de Valdeconejos	VALDECON	-4.06	40.86	1380	611	-56	667	44	8	EPD	Morales-Molino et al., (2017a)
Atxuri	ATXURI01	-1.55	43.25	500	6877	495	6382	33	2	EPD	Penalba (1994); Penalba and Garmendia (1989)
Ayoó de Vidriales	AYOO	-6.07	42.13	780	11846	-26	11872	63	15	EPD	Morales-Molino & García-Antón (2014)
Basa de la Mora	BSM08	0.33	42.55	1906	9856	184	9672	135	16	author	Pérez-Sanz et al., (2013)
Bassa Nera	BSN6	0.92	42.64	1891	9599	-55	9654	62	8	author	Garces-Pastor et al., (2017)
Bermu Mire	BERMU	-4.15	39.43	783	1192	-25	1217	38	8	author	Luelmo-Lautenschlaeger et al., (2018a)
Borreguil de la Caldera	BdIC-01	-3.32	37.05	2992	1440	-56	1496	80	6	author	Ramos-Román et al., (2016)

Bosc dels Estanyons	BOSCESTA	1.63	42.48	2180	11761	26	11735	91	8	EPD	Miras et al., (2007); De Beaulieu et al., (2005)
Botija Bog	BOTIJA	-4.7	39.6	755	3773	82	3691	25	4	author	Luelmo-Lautenschlaeger et al., (2018b)
Cañada de la Cruz	CANCRUZ	-2.69	38.07	1595	9413	-6	9419	39	14	EPD	Yll et al., (1997)
Cala'n Porter	CPORTER	4.13	39.87	24	8809	4802	4007	86	4	EPD	Yll et al., (1994, 1995)
Cala Galdana	GALDANA	3.96	39.94	47	8498	4830	3668	101	5	EPD	López-Merino et al., (2012)
Campo Lameiro	PRD4	-8.52	42.53	260	11948	-11	11959	42	6	EPD	Carrión et al., (2007)
Canada del Gitano_Sierra de Baza	SBAZA	-2.7	37.23	1900	8460	103	8357	111	8	EPD	Cerrillo Cuenca et al., (2007); Cerrillo Cuenca & González Cordero (2011)
Canaleja	CANALEJA	-2.45	40.9	1029	11544	5515	6029	6	2	EPD	Carrion et al., (2001)
Castello Lagoon	Castello Lagoon core EM	3.1	42.28	2	4944	307	4637	85	10	author	Ejarque et al., (2016)
Cha das Lameiras	LAMEIRAS	-7.68	40.94	950	11982	539	11443	32	8	author	Burjachs & Expósito (2015)
Charco da Candieira	CANDIEIR	-7.58	40.34	1409	11970	32	11938	230	31	EPD	Mariscal Alvarez et al., (1983)
Creixell	CreixellIT	1.43	41.16	1	6438	723	5715	32	2	EPD	López-Sáez et al., (2013)
Cueto de la Avellanosa	CUETOAV	-4.36	43.12	1320	6969	292	6677	34	3	EPD	López-Sáez et al., (2017)
Culazón	CULAZON	-4.49	43.23	592	3895	-44	3939	69	11	EPD	van der Knaap & van Leeuwen (1984, 1995, 1997)
El Brezosa	BREZOSA	-4.36	39.35	733	3958	-16	3974	68	11	author	Burjachs & Expósito (2015); Burjachs et al., (1997)
El Carrizal	CARRIZAL	-4.14	41.32	860	9851	0	9851	50	6	EPD	Morales-Molino et al., (2018)
El Maíllo mire	MAI	-6.21	40.55	1100	10687	91	10596	104	10	EPD	Franco-Múgica, et al., (2005)
El Payo	ELPAYO	-6.77	40.25	1000	571	-56	627	50	6	EPD	Morales-Molino et al., (2013)
El Perro mire	ELPERRO	-4.76	39.05	690	4694	-69	4763	41	10	author	Abel Schaad et al., (2009); Silva-Sánchez et al., (2016)
El Portalet	PORTALET	-0.4	42.8	1802	11838	2128	9710	207	13	author	Luelmo-Lautenschlaeger (2019a, 2019b)
El Redondo	REDONDO	-5.66	40.22	1765	3222	31	3191	60	4	author	González-Sampéris et al., (2006)
El Sabinar	SABINAR	-2.12	38.2	1117	6580	1140	5440	129	9	EPD	López-Sáez et al., (2016)
El Tiemblo	TIEMBLO	-4.53	40.36	1250	3184	3	3181	60	9	author	Carrión et al., (2004)
Elx	ELX	-0.75	38.17	1	9903	3392	6511	79	4	EPD	López-Sáez et al., (2018a)

Enol	ENOL	-4.99	43.27	1075	10910	2487	8423	30	7	author	Moreno et al., (2011)
Es Grau	ESGRAU	4.26	39.95	2	7648	-13	7661	98	15	EPD	Burjachs et al., (2017)
Espinosa de Cerrato	CERRATO	-3.94	41.96	885	11578	822	10756	157	7	author	Múgica et al., (2001); Morales-Molino et al., (2017b)
Estanilles	ESTANILLES	1.3	42.63	2247	11908	7646	4262	57	11	EPD	Pérez-Obiol et al., (2012)
Estanya	Estanya Catena	0.53	42.03	677	11882	-37	11919	48	21	author	González-Sampérez et al., (2017); Morellón et al., (2011)
Fuente de la Leche	LECHE	-5.06	40.35	1382	2783	-18	2801	58	10	author	Robles-López et al., (2018)
Fuente del Pino Blanco	PINOBLANCO	-4.98	40.24	1343	653	-38	691	96	5	author	Robles-López et al., (2018)
Hinojos Marsh	HINOJOS	-6.39	36.96	2	4737	2682	2055	46	5	author	López-Sáez et al., (2018b)
Hort Timoner	HTIMONER	4.13	39.88	40	8686	5089	3597	46	4	EPD	Yll et al., (1997)
Hoya del Castillo	N-CAS	-0.16	41.48	258	10740	5629	5111	34	3	EPD	Davis & Stevenson (2007)
La Cruz	LACRUZ	-1.87	39.99	1024	1521	12	1509	23	2	EPD	Burjachs (1996)
La Molina mire	MOLINAE	-6.33	43.38	650	4482	388	4094	152	6	author	López-Merino et al., (2011)
Labradillos Mire	LABRADILLOS	-4.57	40.34	1460	1447	184	1263	25	5	author	Robles López et al., (2017)
Lago de Ajo	LAGOAJO	-6.15	43.05	1570	11755	2175	9580	44	6	EPD	McKeever et al., (1984); Allen et al., (1996)
Lagoa Comprida 2	LAGOA_CO	-7.64	40.36	1650	9863	94	9769	68	4	EPD	Janssen & Woldringh (1981); Moe & Van Der Knaap (1990); Van Den Brink & Janssen (1985)
Lagoa Travessa	TRAVESS1	-8.77	38.3	3	8174	3617	4557	65	4	EPD	Mateus (1985); Mateus (1989)
Laguna de la Mosca	LdIMo composite	-3.31	37.06	2889	8344	-63	8407	68	18	author	Manzano et al., (2019)
Laguna de la Mula	LdIM 10-02	-3.42	37.06	2497	4581	-60	4641	32	8	author	Jiménez-Moreno et al., (2013)
Laguna de la Roya	LAROYA	-6.77	42.22	1608	11927	-41	11968	54	7	PANGAE A	Allen et al., (1996)
Laguna de Rio Seco	Laguna de Rio Seco core 1	-3.35	37.05	3020	10455	-54	10509	69	13	author	Anderson et al., (2011)
Laguna Guallar	N-GUA	-0.23	41.41	336	10654	8056	2598	30	6	EPD	Davis & Stevenson (2007)
Laguna Mesagosa	LAGMESAG	-2.81	41.97	1600	11981	-48	12029	90	5	EPD	Engelbrechten (1999)
Laguna Negra	LAGNEGRA	-2.85	42	1760	11253	-48	11301	68	9	EPD	Engelbrechten (1999)
Laguna Salada Chiprana	N-SAL	-0.17	41.23	150	6872	-40	6912	39	4	EPD	Valero-Garces et al., (2000)

Lake Banyoles	BANYOLES_1, Banyoles SB2	2.75	42.13	174	11952	3316	8636	141	15	EPD	Pèrez-Obiol & Julià (1994); Revelles et al., (2015)
Lake Saloio	SALOIO	-9.02	39.61	70	2804	313	2491	24	2	EPD	Gomes (2011)
Lanzahíta	LANZBOG	-4.94	40.22	558	2657	-51	2708	51	8	author	López-Sáez et al., (1999, 2010)
Las Animas Mire	ANIMAS	-5.03	36.69	1403	797	-57	854	48	10	author	Alba-Sánchez et al., (2019)
Las Lanchas	LANCHAS	-4.89	39.59	800	374	-8	382	20	2	author	Luelmo-Lautenschlaeger et al., (2018c)
Las Pardillas	LASPARDI	-3.03	42.03	1850	10954	404	10550	74	4	EPD	Goñi & Hannon (1999)
Las Vinuelas	VINUELAS	-4.49	39.37	761	4210	-56	4266	58	9	author	Morales-Molino et al., (2019)
Les Palanques	PALANQUES	2.44	42.16	460	10011	524	9487	77	3	EPD	Revelles et al., (2018)
Manaderos	Manaderos core	-4.69	40.34	1292	1293	37	1256	59	9	author	Robles-López et al., (2020)
Marbore	Marbore composite	0.04	42.7	2612	11683	-18	11701	61	18	author	Leunda et al., (2017)
Monte Areo mire	AREO	-5.77	43.53	200	11547	-35	11582	55	12	EPD	López-Merino et al., (2010)
Montes do Buio Cuadramón	CUAII	-7.53	43.47	700	11347	241	11106	19	4	EPD	González et al., (2000)
Navamuno	Navamuno_S 3	-5.78	40.32	1505	11971	-28	11999	207	12	author	López-Sáez et al., (2020)
Navarrés	NAVA1, NAVARRE3	-0.68	39.1	225	11104	3131	7973	72	15	EPD	Carrion & Dupre (1996); Carrión & Van Geel (1999)
Ojos del Tremendal	Ojos del Tremendal core 1	-2.04	40.54	1650	11875	1253	10622	52	4	author	Stevenson (2000)
Patateros bog	PATATERO	-4.67	39.6	700	2655	-19	2674	28	4	EPD	Dorado-Valiño et al., (2014)
Peña Negra	PENANEGR	-5.79	40.33	1000	3434	-62	3496	63	7	EPD	Stefanini (2008)
Pedrido	PEDRIDO	-7.07	43.44	770	5256	106	5150	71	30	EPD	Mighall et al., (2006)
Pena de Cadela	CADELA	-7.17	42.83	970	5233	-14	5247	91	9	EPD	Abel-Schaad & López-Sáez (2013)
Pico del Sertal	SERTAL	-4.44	43.22	940	5200	106	5094	9	3	EPD	Mariscal Alvarez (1986)
Pla de l'Estany	PLAESTANY	2.54	42.19	520	3577	-37	3614	43	4	EPD	Burjachs (1994)
Planell de Perafita	PERAFITA	1.57	42.48	2240	10244	-1	10245	56	11	EPD	Miras et al., (2010)
Posidonia Lligat	LLIGAT	-3.29	42.29	-3	779	15	764	32	5	EPD	López-Sáez et al., (2009)
Pozo de la Nieve	PozoN_2015 core	-4.55	40.35	1600	2258	-37	2295	41	10	author	Robles-López et al., (2017)

Praillos de Bossier Mire	BOSSIER	-4.07	36.91	1610	3428	4	3424	25	3	EPD	Abel-Schaad et al., (2017)
Prat de Vila	PRATVILA	1.43	38.92	4	10776	538	10238	29	5	EPD	Burjachs et al., (2017)
Puerto de Belate	BELATE01	-2.05	43.03	847	8457	1746	6711	60	3	EPD	Penalba (1994); Penalba and Garmendia (1989)
Puerto de las Estaces de Trueba	ESTACAS	-3.7	43.12	1160	6263	391	5872	9	3	PANGAE A	Mariscal (1989)
Puerto de Los Tornos	TORNOS01	-3.43	43.15	920	8718	-34	8752	47	4	EPD	Penalba and Garmendia (1989)
Puerto de Serranillos	SERRANIL	-4.93	40.31	1700	2254	-50	2304	34	5	EPD	López-Merino et al., (2009)
Quintanar de la Sierra	QUINTA02	-3.02	42.03	1470	11995	1953	10042	37	20	EPD	Penalba (1994); Penalba and Garmendia (1989)
Roquetas de Mar	ROQUETAS	-2.59	36.79	0	6910	1057	5853	32	3	EPD	Yll et al., (1995); Cano Villanueva (1997); Pantaléon-Cano (2003); Obiol (1994)
Salada Pequeña	N-PEQ	-0.22	41.03	357	4350	669	3681	43	5	EPD	Davis (2010)
Saldropo	SALDROPO	-2.72	43.05	625	7577	403	7174	76	3	EPD	Penalba (1994, 1989)
Salines playa-lake	SALINES	-0.89	38.5	475	11905	1394	10511	74	7	EPD	Burjachs et al., (2017)
San Rafael	SANRAFA	-2.6	36.77	0	10846	-30	10876	134	6	EPD	Cano Villanueva (1997); Pantaléon-Cano et al., (2003); Yll et al., (1995)
Sanabria Marsh	SANABRIA	-6.73	42.1	1050	11832	0	11832	79	9	EPD	Allen et al., (1996); Hannon (1985); Turner & Hannon (1988)
Serra Mitjana Fen	MITJANA	1.58	42.47	2406	1490	412	1078	15	2	EPD	Miras et al., (2015)
Serrania de las Villuercas	VILLUERCAS	-5.4	39.48	1000	4156	128	4028	31	4	author	Gil-Romera et al., (2008)
Sierra de Gádor	GADOR	-2.92	36.9	1530	6222	1195	5027	86	6	EPD	Carrión et al., (2003)
Siles Lake	SILES	-2.5	38.4	1320	11527	189	11338	67	12	EPD	Carrión (2002)
Tubilla del Lago	TUB	-3.57	41.81	900	7436	31	7405	88	13	EPD	Morales-Molino et al., (2017b)
Turbera de La Panera Cabras	PANERA	-5.76	40.17	1648	164	-56	220	23	2	EPD	Abel Schaad et al., (2009)
Valdeyernos bog	VALDEYER	-4.1	39.44	850	3160	-60	3220	25	4	EPD	Dorado-Valiño et al., (2014)
Valle do Lobo Ribeira de Carcavai	VdL PB2	-8.07	37.06	2	8331	16	8315	144	20	author	Schneider et al., (2010, 2016)
Verdeospesoa mire	VERDEOSPES OA	-2.86	43.06	1015	11137	0	11137	91	12	author	Pérez-Díaz & López-Sáez (2017)

Vilamora Ribeira de Quarteira	Vilamora P01-5	-8.14	37.09	4	3851	919	2932	30	12	author	Schneider et al., (2010, 2016)
Villaverde	VILLAVERDE	-2.37	38.8	870	8066	0	8066	104	9	EPD	Carrión et al., (2001)
Xan de Llamas	XL	-6.32	42.3	1500	4113	34	4079	33	4	EPD	Morales-Molino et al., (2011)
Zoñar	ZONARcombined	-4.69	37.48	300	3234	-45	3279	52	17	author	Martín-Puertas et al., (2008)



918 Table 2. Leave-out cross-validation (with geographically and climatically close sites  
 919 removed) fitness of the modified version of fxTWA-PLS, for mean temperature of the coldest  
 920 month (MTCO), mean temperature of the warmest month (MTWA) and plant-available  
 921 moisture ( $\alpha$ ), with p-spline smoothed fx estimation, using bins of 0.02, 0.02 and 0.002,  
 922 showing results for all the components. RMSEP is the root-mean-square error of prediction.  
 923  $\Delta$ RMSEP is the per cent change of RMSEP using the current number of components than  
 924 using one component less.  $p$  assesses whether using the current number of components is  
 925 significantly different from using one component less, which is used to choose the last  
 926 significant number of components (indicated in bold) to avoid over-fitting. The degree of  
 927 overall compression is assessed by linear regression of the cross-validated reconstructions  
 928 onto the climate variable,  $b_1$ ,  $b_1.se$  are the slope and the standard error of the slope,  
 929 respectively. The closer the slope ( $b_1$ ) is to 1, the less the overall compression is.  
 930  
 931

	ncomp	$R^2$	avg. bias	max. bias	min. bias	RMSEP	$\Delta$ RMSEP	$p$	$b_1$	$b_1.se$
MTCO	1	0.70	-0.86	25.23	0.00	5.20	-39.97	0.001	0.89	0.01
	2	0.73	-0.73	25.00	0.00	4.87	-6.29	0.001	0.91	0.01
	3	0.74	-0.71	24.38	0.00	4.86	-0.32	0.001	0.91	0.01
	<b>4</b>	<b>0.75</b>	<b>-0.59</b>	<b>24.27</b>	<b>0.00</b>	<b>4.70</b>	<b>-3.26</b>	<b>0.001</b>	<b>0.91</b>	<b>0.01</b>
	5	0.74	-0.63	34.54	0.00	4.77	1.51	1.000	0.91	0.01
MTWA	1	0.52	-0.29	17.13	0.00	3.72	-26.88	0.001	0.69	0.01
	2	0.56	-0.14	17.20	0.00	3.53	-5.06	0.001	0.71	0.01
	3	0.56	-0.13	17.01	0.00	3.53	-0.20	0.008	0.71	0.01
	<b>4</b>	<b>0.57</b>	<b>-0.11</b>	<b>17.30</b>	<b>0.00</b>	<b>3.47</b>	<b>-1.56</b>	<b>0.001</b>	<b>0.71</b>	<b>0.01</b>
	5	0.57	-0.11	17.34	0.00	3.48	0.10	0.780	0.71	0.01
$\alpha$	1	0.65	-0.014	0.787	0.000	0.165	-39.59	0.001	0.76	0.01
	2	0.68	-0.016	0.781	0.000	0.159	-3.55	0.001	0.77	0.01
	<b>3</b>	<b>0.68</b>	<b>-0.017</b>	<b>0.757</b>	<b>0.000</b>	<b>0.158</b>	<b>-0.61</b>	<b>0.023</b>	<b>0.78</b>	<b>0.01</b>
	4	0.69	-0.017	0.784	0.000	0.158	-0.43	0.108	0.79	0.01
	5	0.69	-0.017	0.850	0.000	0.158	0.26	0.985	0.80	0.01

932

933 Table 3. Canonical Correspondence Analysis (CCA) result of modern and fossil-  
 934 reconstructed MTCO, MTWA and  $\alpha$ . The summary statistics for the ANOVA-like  
 935 permutation test (999 permutations) are also shown. VIF is the variance inflation factor, Df is  
 936 the number of degrees of freedom,  $\chi^2$  is the constrained eigenvalue (or the sum of constrained  
 937 eigenvalues for the whole model), F is significance, and Pr (>F) is the probability. The CCA  
 938 plots can be found in the Supplementary (Fig. S11).  
 939

Modern	<b>Axes</b>	<b>Axis 1</b>	<b>Axis 2</b>	<b>Axis 3</b>	<b>VIF</b>
	Constrained eigenvalues	0.3819	0.1623	0.1087	/
	<b>Correlations of the environmental variables with the axes:</b>				
	MTCO	-0.815	0.579	0.012	1.31
	MTWA	-0.700	-0.203	0.685	3.34
	$\alpha$	0.883	0.430	-0.187	3.39
		<b>Df</b>	<b><math>\chi^2</math></b>	<b>F</b>	<b>Pr (&gt;F)</b>
	Whole model	3	0.6530	78.113	0.001
	MTCO	1	0.3082	110.597	0.001
	MTWA	1	0.1602	57.489	0.001
	$\alpha$	1	0.1846	66.252	0.001
	CCA 1	1	0.3819	137.076	0.001
	CCA 2	1	0.1623	58.252	0.001
	CCA 3	1	0.1087	39.011	0.001
Fossil-reconstructed	<b>Axes</b>	<b>Axis 1</b>	<b>Axis 2</b>	<b>Axis 3</b>	<b>VIF</b>
	Constrained eigenvalues	0.3601	0.2266	0.2037	/
	<b>Correlations of the environmental variables with the axes:</b>				
	MTCO	0.430	0.776	0.462	1.34
	MTWA	0.987	0.141	-0.076	5.40
	$\alpha$	-0.947	0.088	-0.308	5.28
		<b>Df</b>	<b><math>\chi^2</math></b>	<b>F</b>	<b>Pr (&gt;F)</b>
	Whole model	3	0.7905	226.98	0.001
	MTCO	1	0.2465	212.34	0.001
	MTWA	1	0.3298	284.07	0.001
	$\alpha$	1	0.2142	184.53	0.001
	CCA 1	1	0.3601	310.19	0.001
	CCA 2	1	0.2266	195.24	0.001
	CCA 3	1	0.2037	175.51	0.001

941 Table 4. Assessment of the significance of anomalies to 0.5 ka through time with latitude and  
 942 elevation. The slope is obtained by linear regression of the anomaly onto the longitude or  
 943 elevation.  $p$  is the significance of the slope (bold parts:  $p < 0.05$ ).  $x_0$  is the point where the  
 944 anomaly is 0 in the linear equation, which indicates longitude or elevation where the anomaly  
 945 changes sign.  
 946

		Longitude (°E)			Elevation (km)		
	age (ka)	slope	$p$	$x_0$	slope	$p$	$x_0$
MTCO (°C)	0.5	0.00	/	/	0.00	/	/
	1.5	-0.07	0.411	-13.02	-0.30	0.411	-1.21
	2.5	-0.15	0.095	-8.56	-0.52	0.179	-0.40
	3.5	-0.13	0.314	-14.83	-0.81	0.142	-0.77
	4.5	-0.12	0.444	-17.28	-0.69	0.319	-1.46
	5.5	-0.24	0.247	-9.49	-0.61	0.503	-1.43
	6.5	-0.18	0.372	-12.74	-0.87	0.293	-0.88
	7.5	-0.15	0.421	-20.39	-1.38	0.080	-0.67
	8.5	-0.03	0.890	-77.87	-1.58	0.065	-0.10
	9.5	0.01	0.954	156.31	-1.79	0.060	0.11
	10.5	0.20	0.474	9.25	-1.38	0.241	-0.64
	11.5	0.23	0.528	13.77	0.12	0.947	36.35
MTWA (°C)	0.5	0.00	/	/	0.00	/	/
	1.5	-0.01	0.862	-26.38	-0.05	0.830	-3.35
	2.5	-0.09	0.137	-2.80	-0.45	0.092	1.19
	3.5	<b>-0.23</b>	<b>0.005</b>	<b>-2.03</b>	-0.40	0.284	1.74
	4.5	<b>-0.21</b>	<b>0.016</b>	<b>-2.01</b>	-0.58	0.126	1.55
	5.5	<b>-0.26</b>	<b>0.011</b>	<b>-2.43</b>	-0.49	0.280	1.53
	6.5	<b>-0.24</b>	<b>0.017</b>	<b>-2.30</b>	-0.62	0.137	1.41
	7.5	<b>-0.26</b>	<b>0.012</b>	<b>-3.02</b>	<b>-1.05</b>	<b>0.019</b>	<b>1.28</b>
	8.5	-0.24	0.061	-2.43	<b>-1.15</b>	<b>0.023</b>	<b>1.57</b>
	9.5	<b>-0.32</b>	<b>0.013</b>	<b>-3.20</b>	-0.44	0.459	1.34
	10.5	-0.18	0.115	-1.23	0.54	0.276	0.44
	11.5	0.13	0.453	-7.25	0.37	0.663	0.22
$\alpha$	0.5	0.00	/	/	0.00	/	/
	1.5	0.00	0.508	8.99	-0.01	0.393	3.40
	2.5	0.00	0.517	-9.89	0.02	0.249	0.19
	3.5	<b>0.01</b>	<b>0.006</b>	<b>-4.91</b>	0.02	0.191	0.28
	4.5	<b>0.01</b>	<b>0.010</b>	<b>-4.60</b>	<b>0.05</b>	<b>0.008</b>	<b>0.79</b>
	5.5	<b>0.01</b>	<b>0.005</b>	<b>-4.75</b>	<b>0.05</b>	<b>0.027</b>	<b>0.67</b>
	6.5	<b>0.01</b>	<b>0.007</b>	<b>-5.34</b>	<b>0.06</b>	<b>0.004</b>	<b>0.60</b>
	7.5	<b>0.02</b>	<b>0.009</b>	<b>-6.05</b>	<b>0.09</b>	<b>0.000</b>	<b>0.75</b>
	8.5	<b>0.01</b>	<b>0.049</b>	<b>-6.67</b>	<b>0.09</b>	<b>0.000</b>	<b>0.88</b>
	9.5	<b>0.01</b>	<b>0.048</b>	<b>-6.40</b>	<b>0.07</b>	<b>0.012</b>	<b>0.70</b>
	10.5	0.01	0.183	-4.85	0.02	0.535	0.59
	11.5	0.00	0.713	-2.76	0.03	0.654	0.93

947

948 **Appendix A**949 **Theoretical basis:**950 **The previous version of fxTWA-PLS (fxTWA-PLS1):**

951 The estimated optimum ( $\hat{u}_k$ ) and unbiased tolerance ( $\hat{t}_k$ ) of each taxon are calculated from  
 952 the modern training data set as follows:

$$953 \quad \hat{u}_k = \frac{\sum_{i=1}^n y_{ik} x_i}{\sum_{i=1}^n y_{ik}} \quad (A1)$$

$$954 \quad \hat{t}_k = \sqrt{\frac{\sum_{i=1}^n y_{ik} (x_i - \hat{u}_k)^2}{(1 - 1/N_{2k}) \sum_{i=1}^n y_{ik}}} \quad (A2)$$

955 where

$$956 \quad N_{2k} = \frac{1}{\sum_{i=1}^n \left( \frac{y_{ik}}{\sum_{i'=1}^n y_{i'k}} \right)^2} \quad (A3)$$

957 where  $n$  is the total number of sites;  $y_{ik}$  is the observed abundance of the  $k^{\text{th}}$  taxon at the  $i^{\text{th}}$   
 958 site;  $x_i$  is the observed climate value at the  $i^{\text{th}}$  site;  $N_{2k}$  is the effective number of occurrences  
 959 for the  $k^{\text{th}}$  taxon.

960 fx correction is applied as weight in the form of  $1/fx^2$  at regression at step 7 in Table 1 in Liu  
 961 et al. (2020). The regression step uses robust linear model fitting by the R code:

$$962 \quad rlm(x_i \sim comp_1 + comp_2 + \dots + comp_{pls}, weights = 1/fx^2) \quad (A4)$$

965 **The modified version of fxTWA-PLS (fxTWA-PLS2):**

966 The distribution of  $y_{ik}$  is influenced by the distribution of the climate variable, so we need to  
 967 apply the fx correction when calculating optimum and tolerance for each taxon as follows:

$$968 \quad \hat{u}_k = \frac{\sum_{i=1}^n \frac{y_{ik} x_i}{f_{x_i}}}{\sum_{i=1}^n \frac{y_{ik}}{f_{x_i}}} \quad (A5)$$

$$969 \quad \hat{t}_k = \sqrt{\frac{\sum_{i=1}^n \frac{y_{ik} (x_i - \hat{u}_k)^2}{f_{x_i}}}{\left(1 - \frac{1}{N_{2k}}\right) \sum_{i=1}^n \frac{y_{ik}}{f_{x_i}}}} \quad (A6)$$

970 where

$$971 \quad N_{2k} = \frac{1}{\sum_{i=1}^n \left( \frac{\frac{y_{ik}}{f_{x_i}}}{\sum_{i'=1}^n \frac{y_{i'k}}{f_{x_{i'}}}} \right)^2} \quad (A7)$$

972 The modified version of fxTWA-PLS applies fx correction separately at taxon calculation  
 973 and regression (step 2 and 7 in Table 1 in Liu et al., 2020), both using weight in the form of  
 974  $1/fx$ . The regression step (step 7) then becomes:

$$975 \quad rlm(x_i \sim comp_1 + comp_2 + \dots + comp_{pls}, weights = 1/fx) \quad (A8)$$

976 The previous version uses  $fx$  values extracted from histograms, and different bin widths may  
977 result in different training results. The modified version applies P-splines histogram  
978 smoothing (Eilers and Marx, 2021) with third order difference penalty, which makes the  $fx$   
979 values almost independent on the bin width. The optimal smoothing parameter of the P-spline  
980 penalty was determined by the HFS (Harville-Fellner-Schall) algorithm (Eilers and Marx,  
981 2021) for the Poisson likelihood for the histogram counts.

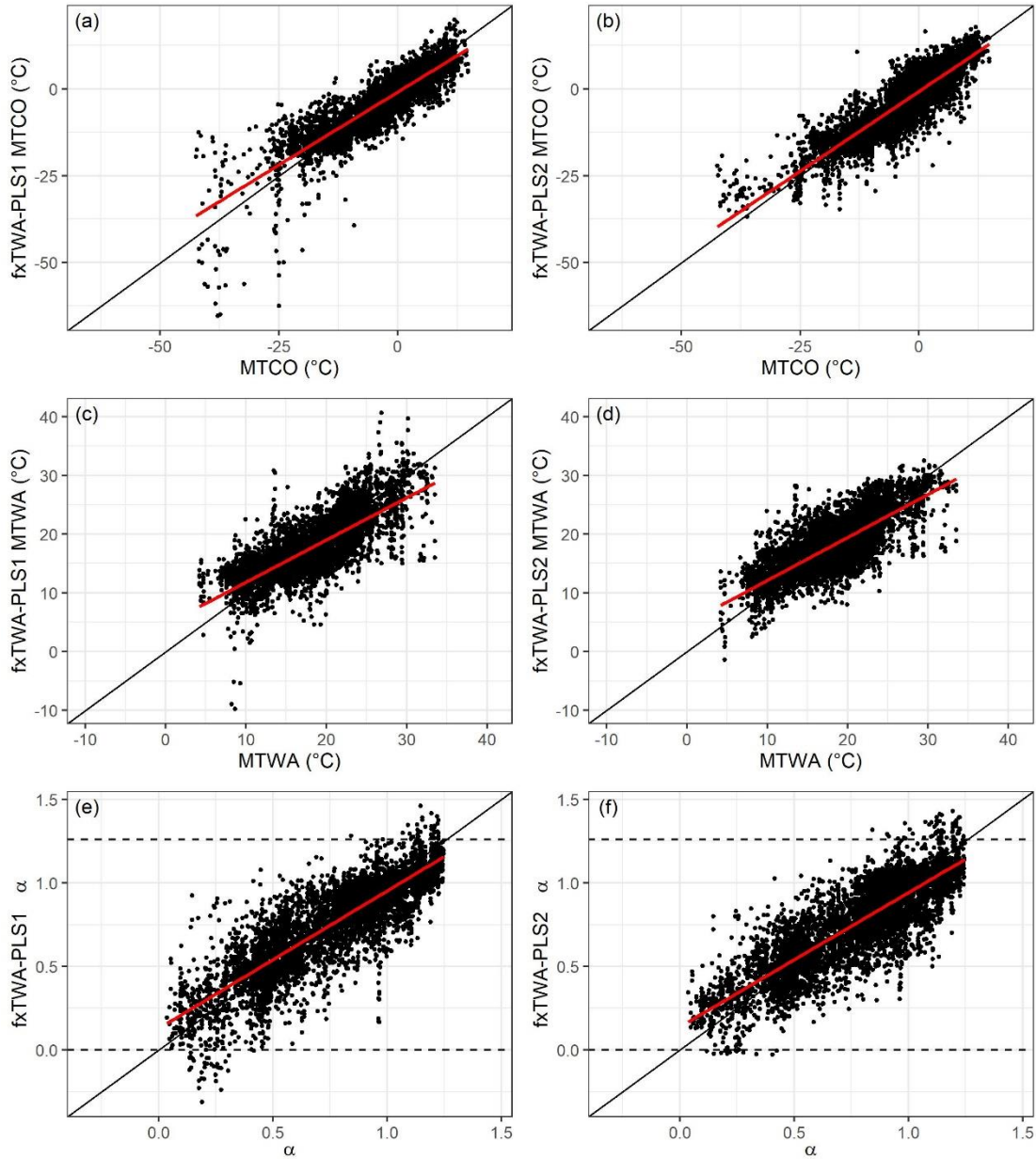
982 Table A1. Leave-out cross-validation (with geographically and climatically close sites removed)  
 983 fitness of the previous and modified version of fxTWA-PLS (fxTWA-PLS1 and fxTWA-PLS2,  
 984 respectively), for mean temperature of the coldest month (MTCO), mean temperature of the warmest  
 985 month (MTWA) and plant-available moisture ( $\alpha$ ), using bins of 0.02, 0.02 and 0.002, respectively.  $n$   
 986 is the number of components used. RMSEP is the root mean square error of prediction.  $\Delta$ RMSEP is  
 987 the per cent change of RMSEP using the current number of components than using one component  
 988 less.  $p$  assesses whether using the current number of components is significantly different from using  
 989 one component less, which is used to choose the last significant number of components (indicated in  
 990 bold) to avoid overfitting. The degree of overall compression is assessed by doing linear regression to  
 991 the cross-validation result and the climate variable.  $b1$ ,  $b1.se$  are the slope and the standard error of  
 992 the slope, respectively. The closer the slope ( $b1$ ) is to 1, the lower the overall compression is. fx  
 993 correction is set intrinsic in functions in `fxTWA` package for both versions in this paper, instead  
 994 of relying on an outside input in Liu et al. (2020), so the values of fxTWA-PLS1 might be slighted  
 995 different from values in Table 3 in Liu et al. (2020), but it doesn't affect the conclusion.  
 996

	Method	$n$	$R^2$	avg. bias	max. bias	min. bias	RMSEP	$\Delta$ RMSEP	$p$	$b1$	$b1.se$
MTCO	fxTWA-PLS1	1	0.66	-0.86	31.17	0.00	5.21	-39.87	0.001	0.76	0.01
		2	0.72	-0.52	36.65	0.00	4.70	-9.78	0.001	0.80	0.01
		3	0.73	-0.47	41.18	0.00	4.62	-1.63	0.001	0.82	0.01
		<b>4</b>	<b>0.73</b>	<b>-0.51</b>	<b>44.86</b>	<b>0.00</b>	<b>4.58</b>	<b>-1.01</b>	<b>0.006</b>	<b>0.82</b>	<b>0.01</b>
		5	0.73	-0.41	58.35	0.00	4.62	0.89	0.708	0.83	0.01
	fxTWA-PLS2	1	0.70	-0.86	25.23	0.00	5.20	-39.97	0.001	0.89	0.01
		2	0.73	-0.73	25.00	0.00	4.87	-6.29	0.001	0.91	0.01
		3	0.74	-0.71	24.38	0.00	4.86	-0.32	0.001	0.91	0.01
		<b>4</b>	<b>0.75</b>	<b>-0.59</b>	<b>24.27</b>	<b>0.00</b>	<b>4.70</b>	<b>-3.26</b>	<b>0.001</b>	<b>0.91</b>	<b>0.01</b>
		5	0.74	-0.63	34.54	0.00	4.77	1.51	1.000	0.91	0.01
MTWA	fxTWA-PLS1	1	0.50	-0.53	17.91	0.00	3.87	-24.09	0.001	0.67	0.01
		<b>2</b>	<b>0.56</b>	<b>-0.54</b>	<b>17.71</b>	<b>0.00</b>	<b>3.52</b>	<b>-8.98</b>	<b>0.001</b>	<b>0.69</b>	<b>0.01</b>
		3	0.57	-0.49	25.14	0.00	3.52	0.09	0.565	0.73	0.01
		4	0.57	-0.43	34.92	0.00	3.56	1.12	0.974	0.75	0.01
		5	0.57	-0.46	32.23	0.00	3.55	-0.23	0.139	0.74	0.01
	fxTWA-PLS2	1	0.52	-0.29	17.13	0.00	3.72	-26.88	0.001	0.69	0.01
		2	0.56	-0.14	17.20	0.00	3.53	-5.06	0.001	0.71	0.01
		3	0.56	-0.13	17.01	0.00	3.53	-0.20	0.008	0.71	0.01
		<b>4</b>	<b>0.57</b>	<b>-0.11</b>	<b>17.30</b>	<b>0.00</b>	<b>3.47</b>	<b>-1.56</b>	<b>0.001</b>	<b>0.71</b>	<b>0.01</b>
		5	0.57	-0.11	17.34	0.00	3.48	0.10	0.780	0.71	0.01
$\alpha$	fxTWA-PLS1	1	0.63	-0.020	0.773	0.000	0.174	-36.23	0.001	0.78	0.01
		2	0.69	-0.012	0.902	0.000	0.157	-9.66	0.001	0.79	0.01
		<b>3</b>	<b>0.69</b>	<b>-0.011</b>	<b>0.820</b>	<b>0.000</b>	<b>0.155</b>	<b>-1.28</b>	<b>0.001</b>	<b>0.79</b>	<b>0.01</b>
		4	0.70	-0.010	0.786	0.000	0.156	0.25	0.867	0.81	0.01
		5	0.70	-0.010	0.786	0.000	0.156	0.09	1.000	0.81	0.01
	fxTWA-PLS2	1	0.65	-0.014	0.787	0.000	0.165	-39.59	0.001	0.76	0.01
		2	0.68	-0.016	0.781	0.000	0.159	-3.55	0.001	0.77	0.01
		<b>3</b>	<b>0.68</b>	<b>-0.017</b>	<b>0.757</b>	<b>0.000</b>	<b>0.158</b>	<b>-0.61</b>	<b>0.023</b>	<b>0.78</b>	<b>0.01</b>
		4	0.69	-0.017	0.784	0.000	0.158	-0.43	0.108	0.79	0.01
		5	0.69	-0.017	0.850	0.000	0.158	0.26	0.985	0.80	0.01

997

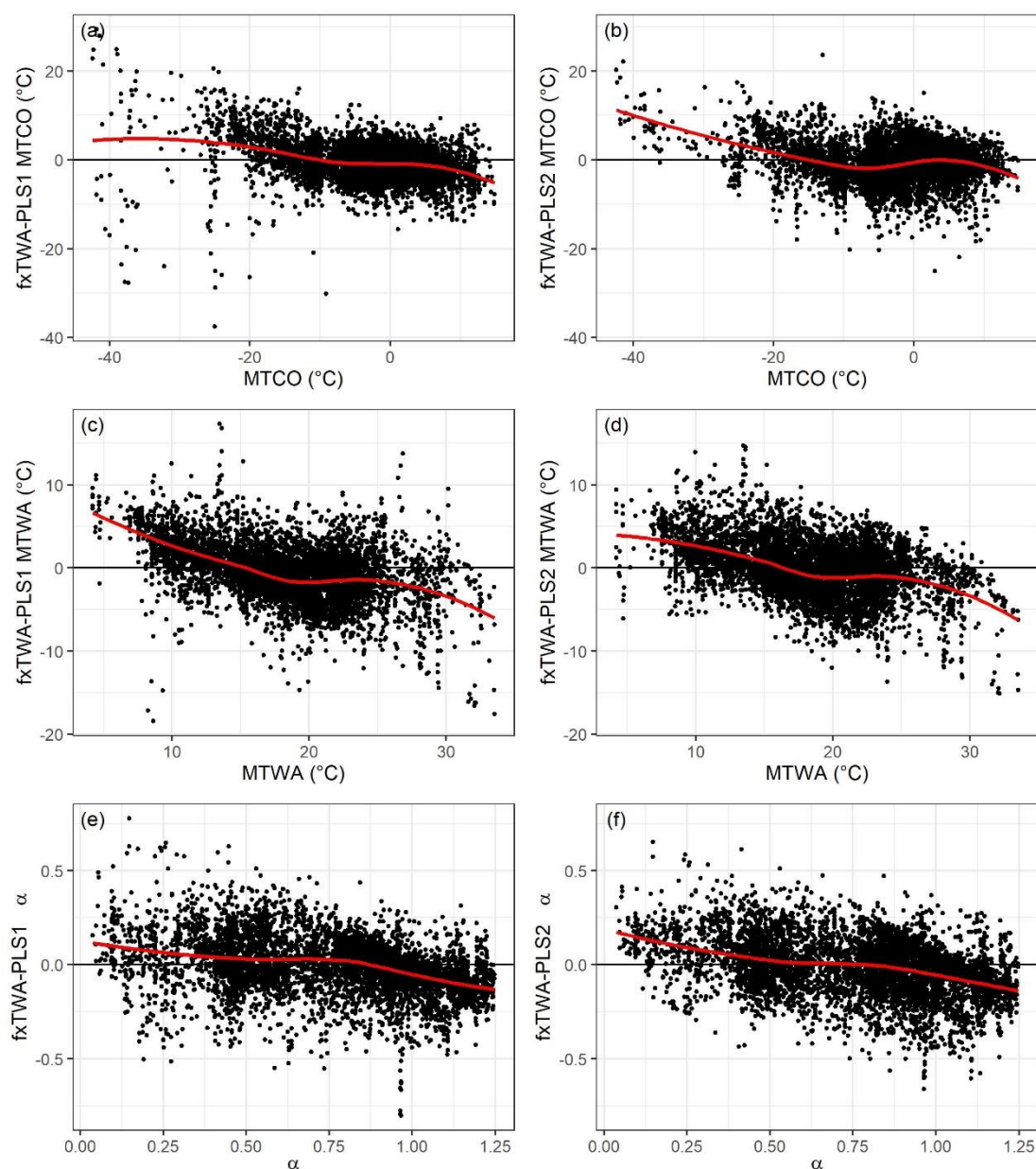
998

999 Figure A1. Training results using the last significant number of components. The left panel  
 1000 shows the previous version (fxTWA-PLS1) and the right panel shows the modified version of  
 1001 fxTWA-PLS (fxTWA-PLS2). The 1: 1 line is shown in black; the linear regression line is  
 1002 shown in red, to show the degree of overall compression. The horizontal dashed lines indicate  
 1003 the natural limit of  $\alpha$  (0~1.26).  
 1004



1005  
 1006

1007 Figure A2. Residuals using the last significant number of components. The left panel shows  
 1008 the previous version (fxTWA-PLS1) and the right panel shows the modified version (fxTWA-  
 1009 PLS2) of fxTWA-PLS. The zero line is shown in black; the locally estimated scatterplot  
 1010 smoothing is shown in red, to show the degree of local compression.  
 1011



1012

1013 As shown in Table A1, Figure A1 and A2, the modified version is able to further reduce the  
 1014 compression in MTCO and MTWA, and maximum bias in MTCO, MTWA and  $\alpha$ . As shown  
 1015 in Figure A1 and A2, there is less scatter and there are less  $\alpha$  values beyond the natural limit.